Univerzita Karlova v Praze
Matematicko-fyzikální fakulta

DIPLOMOVÁ PRÁCE

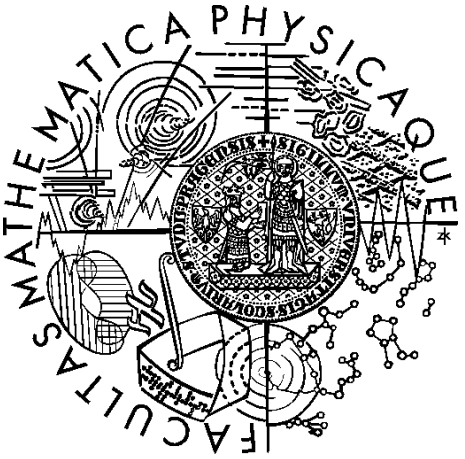

Lukáš Chlad

HADES - STUDIUM ZMĚN VLASTNOSTÍ HADRONŮ

Ústav částicové a jaderné fyziky

Vedoucí diplomové práce: RNDr. Andrej Kugler, CSc.
Studijní program: Fyzika
Studijní obor: Jaderná a subjaderná fyzika

Praha 2015

Charles University in Prague
Faculty of Mathematics and Physics

MASTER THESIS

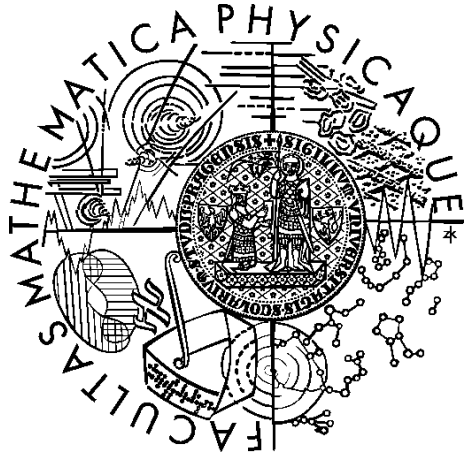

Lukáš Chlad

HADES - STUDY OF CHANGES OF HADRON'S PROPERTIES

Institute of Particle and Nuclear Physics

Supervisor of the master thesis: RNDr. Andrej Kugler, CSc.

Study programme: Physics

Specialization: Nuclear and Subnuclear Physics

Prague 2015

Acknowledgements

At this point I would like to express my gratitude to my supervisor Dr. Andrej Kugler for his support and fruitful discussions. Then I want to thank the colleagues from Nuclear Physics Institute at Řež namely Dr. Pavel Tlustý and Dr. Ondřej Svoboda for their assistance and advices with data analysis. I appreciate the help from Jacek Biernat and Dr. Piotr Salabura with the introduction into simulations for HADES detector. Thanks also to all members of HADES collaboration who were always very kind and open for discussions.

I will never forget all the experiences from the Summer Student Program at GSI in summer 2014 as well as I will be always grateful to Dr. Jerzy Pietraszko who was mentor of my project.

I am very grateful to Dr. Alice Valkárová for the help with organization of two study stays abroad.

Last but not least I would like to thank my family and friends for their moral support and help in every life situation.

This work was supported by Specific Academic Research Projects of Charles University in Prague number 114-09/260097 and 114-09/260219, GSI, GACR 13-06759S and AS CR M100481202 grants, and by European Community FP7 – Capacities, contract HadronPhysics3 n. 283286.

I declare that I carried out this master thesis independently, and only with the cited sources, literature and other professional sources.

I understand that my work relates to the rights and obligations under the Act No. 121/2000 Coll., the Copyright Act, as amended, in particular the fact that the Charles University in Prague has the right to conclude a license agreement on the use of this work as a school work pursuant to Section 60 paragraph 1 of the Copyright Act.

In Prague date ..... signature of the author

Název práce: HADES - STUDIUM ZMĚN VLASTNOSTÍ HADRONŮ

Autor: Lukáš Chlad

Ústav: Ústav částicové a jaderné fyziky

Vedoucí diplomové práce: RNDr. Andrej Kugler, CSc., Ústav jaderné fyziky AV ČR, v.v.i.

Abstrakt: V průběhu léta 2014 měla kolaborace detektoru HADES možnost měřit interakce pionů s různými jádry. Byly vytyčeny dva hlavní cíle měření. Prvním z nich byl výzkum hadronů s s-kvarkem a jejich chování v prostředí s normální jadernou hustotou. Tato analýza se především zaměřila na mezon ϕ a baryon Λ. Druhý cíl měření se soustředil na vlastnosti baryonových rezonancí v oblasti N(1520) a N(1535). Zvláštní pozornost je v práci věnována svazkovým detektorům, které využívají různé metody detekce částic. Zejména jsou diskutovány detektory Hodoskop a START. Dále je obsahem práce analýza $\pi + \mathrm{p}$ elastického rozptylu, která je důležitá zejména pro normalizaci účinného průřezu. Získané hodnoty výtěžku elastického rozptylu jsou porovnány se simulacemi a publikovanými daty.

Klíčová slova: hadrony, di-leptony, HADES

Title: HADES - STUDY OF CHANGES OF HADRON'S PROPERTIES

Author: Lukáš Chlad

Department: Institute of Particle and Nuclear Physics

Supervisor: RNDr. Andrej Kugler, CSc., Nuclear Physics Institute of the ASCR, public research institution

Abstract: During the summer 2014, the HADES collaboration had the opportunity to measure pion collisions with different nuclei. These measurements were done with two objectives. The first being the investigations of hadrons with strange quarks and their behaviour at normal nuclear density. The analysis of this will concentrate specifically on ϕ meson and Λ baryon production. The focus on properties of baryonic resonances in the region of N(1520) and N(1535) formed the second objective. Special emphasis is put on beam line detectors which use different particle detection techniques. In particular, the scintillator based Hodoscope and diamond based Start detector will be discussed. There is also presented the analysis of $\pi + \mathrm{p}$ elastic scattering which is important for normalisation of the cross section of the reactions of interest. The measured elastic scattering yields are compared with dedicated simulations and previously published data.

Keywords: hadrons, di-leptons, HADES

Contents

Introduction

The centre of interest of this thesis is the experiment with negative pion beam measured by HADES spectrometer at GSI, Darmstadt, Germany. This measurement was done during the summer 2014 but the preparations in Nuclear Physics Institute at Řež (NPI) started already at autumn 2013. At that time also my studies for master degree started and so I had the chance to participate on the preparation works whole time. As it is nowadays usual in particle and nuclear physics the tasks are distributed to all collaboration which in HADES case include around 150 people. I could not measure everything myself but at most times I was present or participated on the measurements. However all the analysis of measured data presented in this thesis is my work. Some pictures presented in this work where taken from presentations or papers written by colleagues from HADES collaboration and it is always mentioned in the figure caption.

In the chapter 1 a short but rather complete description of HADES spectrometer is presented. The functionality and structure of all important subdetectors is given.

Continuing with the description of the beam line detectors used during the pion beam experiment in chapter 2. The special attention is put on the scintillator based hodoscopes that were prepared in NPI. A lot of test were performed to make sure that the detector will be ready for the application with pion beam.

Next chapter 3 is dedicated to START detector as another beam line detector. Mine task was preparing time calibration parameters and to determine time resolution of START detector. Two procedures of time calibration are presented together with the results on time resolution of START, TOF, RPC and Hodoscope detectors.

The last chapter 4 contains the analysis of elastic scattering $\pi^- p \to \pi^- p$. Our motivation for analysing this reaction channel is explained. The results of differential cross section are compared with simulations and published data. Also the reconstruction of pion momentum with HADES is tested with the kinematics of the elastic scattering.

CHAPTER 1

HADES experiment

With aim to study changes of properties (mass, mean life time etc.) of the light vector mesons ρ, ω, ϕ the **H**igh-**A**cceptance **DiE**lectron **S**pectrometer (in next HADES) was built in GSI Helmholtzzentrum für Schwerionenforschung in Darmstadt, Germany, during the 90's [1]. The light vector mesons were studied previously in DLS experiment at accelerator Bevalac in Berkeley, California USA, for their short life time compared to the duration of compression phase of relativistic heavy ion reaction in energetic range $1 \div 2$ AGeV. Another important property of these mesons is their electromagnetic decay into $e^- + e^+$ leptons that do not interact via strong interaction, i.e. they can provide undistorted information about the hadronic matter. HADES's physics program contains above mentioned relativistic heavy ion collision as well as proton or pion collision with fixed target.

Compared with pioneering DLS experiment HADES has much better invariant mass resolution $\Delta M/M \approx 1\%$ and also geometrical acceptance (85% in azimuth angle and interval $18° < \theta < 85°$ in polar angle). Also high granularity and faster electronics contributes to better physical results. HADES is in azimuth angle divided into six identical sectors and contains several subdetectors that are described below in more details. Beside these there will be also mentioned beam detectors which were used for pion beam last year. One can see the disposition of subdetectors on figure 1.1.

1.1 Target

It was already mentioned that HADES is a fix target experiment [2]. In most cases the target is segmented into several cylinders that are glued to a foil which is fix to the support structure. All of this is then placed into the beam pipe and the air is pulled out. Interaction probability of beam particles with target is approximately 1 %. The material used as target depends on the physics program, e.g. LH_2, carbon, polyethylene, niobium, tungsten or gold.

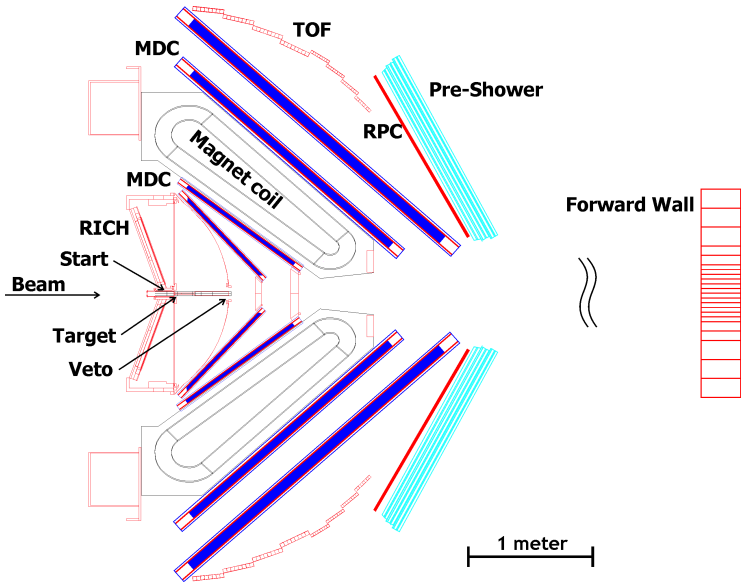

Figure 1.1: Cross-section of HADES spectrometer. Taken from [3].

1.2 Detector START

The START detector is a diamond based detector for measuring t_0 for the final time of flight for individual particles [2]. Position of the START detector is in front of the target inside the beam pipe in the order of tens centimetres. The radiation in this place is very intensive but still is cause only small damage in the diamond material [5]. Another application of this detector is beam monitoring. Usually there is also the VETO detector, very similar to START only behind the target which is used in trigger logic for better event selection. Both these detectors are made from poly-crystalline diamond, or in more recent experiments mono-crystalline, made by process called Chemical Vapour Deposition (CVD). The thickness of the diamond plates is between 50 μm and 500 μm depending on the energy losses of beam particles in diamond material [4]. Diamonds are covered with very thin layers of metal (chrome, gold, platinum etc.) that are used as electrodes. Collected signals from the diamond with electrodes are amplified with low-noise and broad-band amplifiers and then the trigger signal is get out of leading edge discriminator.

The advantage of the diamond material is in very large energy gap between valence and conducting level (band gap = 5.5 eV), this means that there is no need for detector cooling and still there will no noise at room temperature. Another advantage is large electron drift velocity (220 km/s) which results in possible good time resolution (well below 50 ps) and high count rate capability (up to 10^8 parts/s/mm^2). Finally, thanks to low $Z = 6$ of carbon and technical opportunity to make very fine diamond plates, there is no problem with multiple scattering with these detectors.

1.3 RICH detector

The **R**ing **I**maging **CH**erenkov detector is used to identify relativistic $e^{\pm}$ [6], i.e. that slow hadrons are not detected. The basic functionality of RICH is based on a discovery that charged particles in medium (n is refractive index of the medium) with speed grater than phase speed of light in that medium emit photons under angle θ_C with respect to their trajectory. This angle is connected with the speed of particle $\beta = \sqrt{1 - \frac{1}{\gamma^2}}$ through the relation

$$\cos\theta = \frac{1}{\beta n}. \tag{1.1}$$

As was mentioned there was a hadron-blind requirement on RICH detector. From simulations was determined the threshold for $\gamma_{\text{tr}} \approx 12$ (based on typical speed of electrons and hadrons emitted from collisions). Between other requirements belongs that the position of photon detectors must be upstream of the target to keep amount of material in electron path as low as possible. This lead to layout which is presented on figure 1.2. As gas radiator was chosen C_4F_{10} with $\gamma_{\text{tr}} = 18$ and with a high transmission for vacuum ultra violet (VUV) wavelength region (up to $\lambda = 145\,\text{nm}$). Emitted Cherenkov light is than reflected on the spherical mirror with radius $R = 871\,\text{mm}$ and continue through the CaF_2 window to detector gas (very pure CH_4). The pads with photon detector (Multi-Wire Proportional Chamber) are inclined by 20° because the position of the target is not exactly in the centre of the spherical mirror. Principle of the photon detection is shown on detail of picture 1.2. There is a certain probability, determined by quantum efficiency, that from collision of photon with the CsI will release electron (photo effect). This electron is attracted to anodic wire and create an avalanche of positive ions which drift back to cathode pad where they are registered. From tests single-electron detection efficiency was determined $\varepsilon \approx 95\%$. Whole RICH detector consists 4712 cathode pads per sector which are read out and in data analysis we look for a ring shapes.

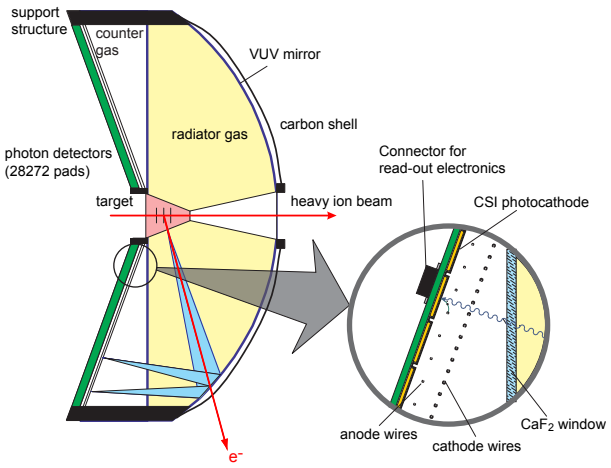

Figure 1.2: RICH detector with detail on photon detector. Taken from [7].

1.4 Magnet

For the purpose of measuring particle momentum there is need of position measurement (in HADES case there are multi-wire drift chambers, see 1.5) in front of and behind the magnetic field. There were put several requirements on the properties of magnetic field:

- provide enough magnetic intensity that enables in combination with MDC momentum resolution for electron better than $\sigma_p/p < 2\%$,
- acceptance in phase space $p = 0.1 \div 2\,\mathrm{GeV/c}$, $18^\circ < \theta < 85^\circ$ and almost full azimuth coverage,
- no magnetic field in RICH subdetector.

From simulations for energy region of the SIS18 accelerator ($1 \div 2\,\mathrm{AGeV}$ depends on the mass of accelerated nuclei) it became clear that we would need transverse momentum kick $p_{\mathrm{kick}} \leq 0.1\,\mathrm{GeV/c}$ for the high-momentum particles [2]. Since there is relation between kick momentum p_{kick}, magnetic field intensity B and length of particle trajectory through the magnetic field L

$$p_{\mathrm{kick}} \sim B \cdot L, \tag{1.2}$$

one gets clear limit for the intensity $B \leq 0.9\,\mathrm{T}$ if we want to keep the spectrometer compact($L \simeq 0.4\,\mathrm{m}$). Subsequently one also get the requirement on MDC subdetector, two planes of chambers on both sides of magnetic field with distance between $d = 0.3\,\mathrm{m}$ and position resolution better than $150\,\mu\mathrm{m}$. To satisfy the demand on zero magnetic field in RICH the toroidal magnetic field was chosen with six superconducting coils places in the vertices of imaginary hexagon, see figure 1.3. Thanks to this geometry there is no additional matter in the particle path which might cause unwanted multiple scattering. Each coil has 140 turns and in full operational mode there is current of 3464 A. To keep the coils in superconducting state there is a need of cooling system. The shielding of coils is cooled by liquid nitrogen at 85 K and the current leads themselves are cooled at 4.7 K with liquid helium. Some problems with cooling might occur if there would be a bubble inside the tubes that lead helium to the coils. To avoid these problems helium is compressed to 0.29 MPa when the critical point of helium at 4.7 K is 0.23 MPa. When the helium gas gets to the coils it expands to 0.13 MPa and is liquefied.

The field map which was calculated (and is displayed on figure 1.4) is in very good agreement with the measurements (after corrections on the Earth magnetic field) which were done with Hall probes and optical position system.

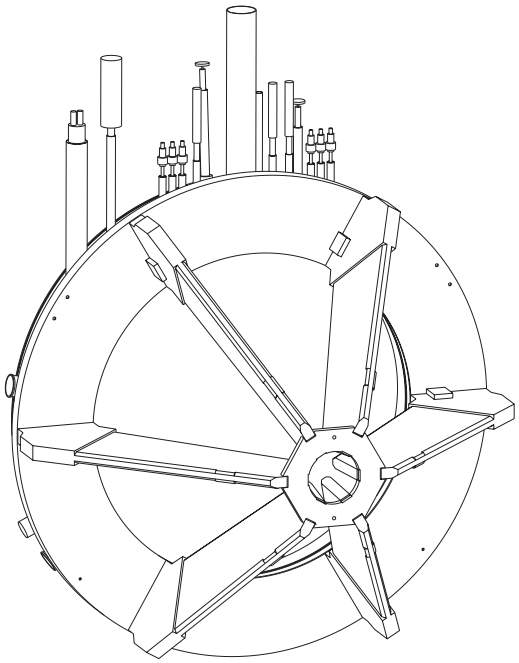

Figure 1.3: Scheme of ILSE (Iron-Less Superconducting Electromagnet) construction. Taken from [3].

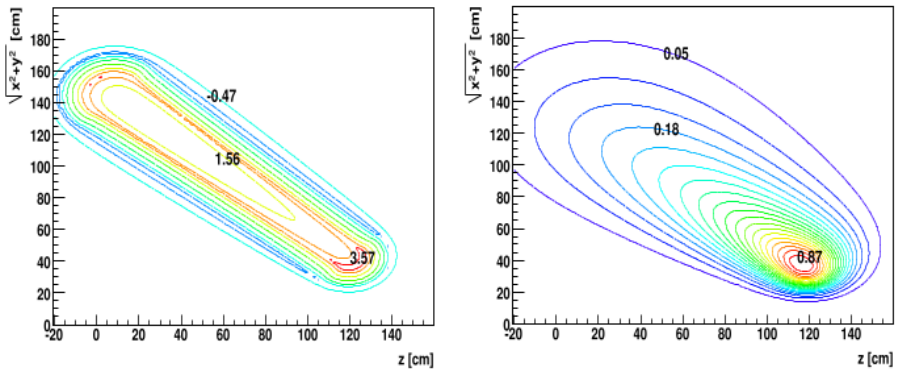

Figure 1.4: Magnetic field in contour lines. Left picture is for $\phi = 30°$ where the coil is placed and right is for $\phi = 0°$. Along the beam we use z-direction. Taken from [2].

1.5 Multi-wire Drift Chambers

As it was already mentioned in section 1.4 the subdetector so called MDC consist from four planes, two in front of magnet and two behind. Also the requirement on position resolution better than 150 μm was mentioned above. Between other demands on detector performance belong especially high efficiency and keeping detector thickness as low as possible in order to restrict multiple scattering (for this reason only very thin Mylar foil is covering the chamber). Shape of the chambers is trapezoidal to fit in the spaces of hexagonal layout of spectrometer, see figure 1.5. On the same figure one can see that in each chamber there are six layers of wires with different orientation ($\pm 0°, \pm 20°, \pm 40°$) [8]. The size of chambers varies from 0.35 m^2 to 3.2 m^2 and each of them is divided to 1100 drift cells. Chambers are filled with mixture of helium and isobutane ($He : C_4H_{10} = 60 : 40$). The diameter of potential and cathode wires (made from aluminium) is between 80 μm and 100 μm, initial tension on these wires is in range $80 \div 120$ cN. Meanwhile the sense wires, the detail of wires disposition see figure 1.6, are made from gold and tungsten with diameter 20 μm (planes I-III) and 30 μm (plane IV) with initial tension $40 \div 110$ cN.

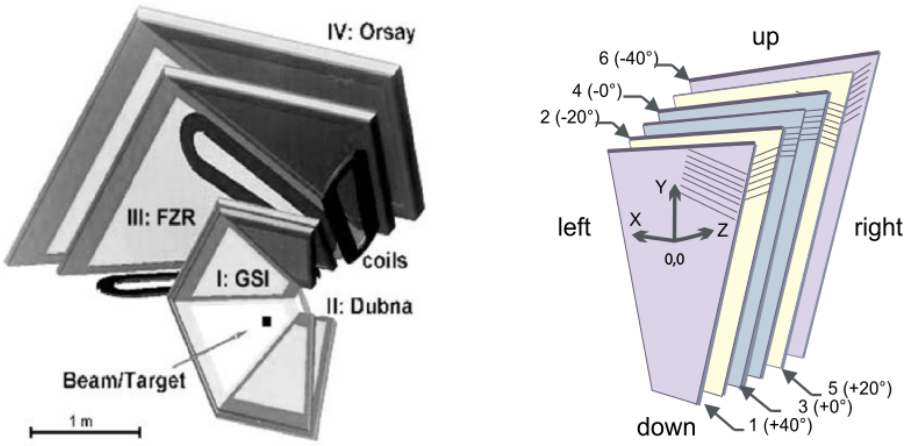

Figure 1.5: On left picture is MDC layout with name of institutions which made the according plane. On right picture is scheme of inner structure of one MDC chamber. Taken from [2].

To achieve desired position resolution it is needed to align the detectors (not only MDC chambers) which is usually done with cosmic rays before beam time and with straight trajectories (without magnetic field). This procedure allows to set the correct position with accuracy of 0.1 mm. The efficiency of particle detection is about 90% for plane I, 97% for plane II and 100% for planes III and IV. Smaller efficiency for first two planes is due to dependence of efficiency on the applied high-voltage. Optimal efficiency is achieved for 2000 V but because of the non-stability of this setting the value of HV is during beam times 1800 V. Because of this effect the efficiency of track reconstruction is 86%. On figure 1.7 is shown the results of time respective position resolution, one can notice that the requirement on position resolution is accomplished.

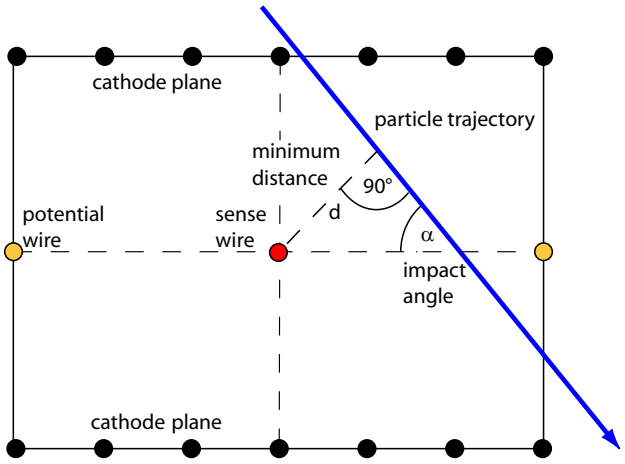

Figure 1.6: Detail on wires disposition with example of particle track. Taken from [3].

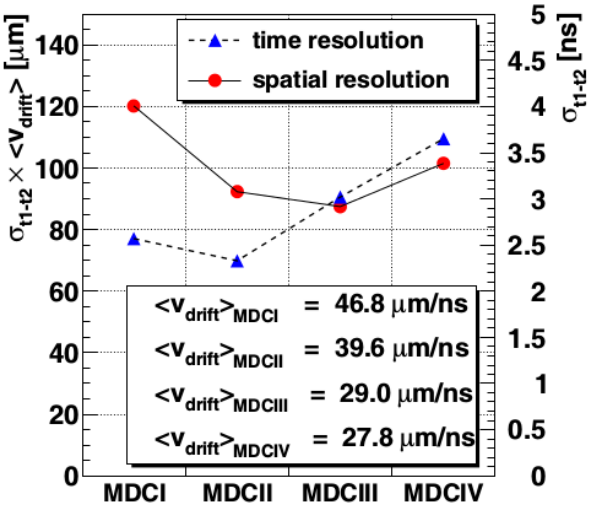

Figure 1.7: Spatial and time resolution for all MDC planes. Taken from [2].

From measurement of time over threshold (ToT, effectively the width of signals) it is possible to get an information about energy losses $^{dE}/_{dx}$ for reconstructed track, i.e. we can get an information about particle momentum p. Relation between ToT and energy losses can be described by

$$\mathrm{ToT} = c_0 + c_1 \left[\log_{10} \left(\frac{\mathrm{d}E}{\mathrm{d}x} + c_3 \right) \right]^{c_2}, \tag{1.3}$$

where c_i for $i = 0, .., 3$ are fit parameters. These parameters were obtained from elastic scattering of proton on proton, see figure 1.8. There is also shown very good agreement of measured data with theoretical calculations from Bethe-Bloch formula.

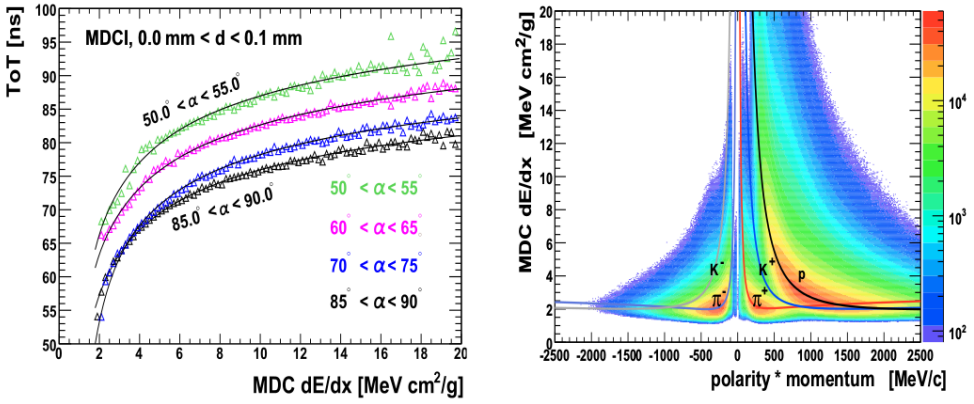

Figure 1.8: Left picture shows results of fitting dependence of ToT on energy losses (for protons and different incidence angles α) according to 1.3. Right picture shows measured energy losses dependent on particle momentum multiplied by its charge sign. Taken from [2].

1.6 Time Of Flight chambers

In order to determine particle identity, i.e. type of particle, one needs to find out rest mass m of this particle. Usually to determine the mass we use formula

$$p = \beta \cdot \gamma \cdot m \cdot c, \tag{1.4}$$

where β and $\gamma = {}^{1}/\sqrt{1-\beta^2}$ are well known relativistic factors and c is speed of light in vacuum. So we need to measure factor $\beta = {}^{v}/_{c}$ or in other words velocity v of the particle and then (as we already know momentum p from MDC measurement) we can calculate the rest mass m. That leads us to the **T**ime-**O**f-**F**light chambers (respectively to the **R**esistive **P**late **C**hambers which are in more detail introduced in section 1.7) which measure time t since START time t_0 and thanks to known distance $s = v \cdot t$ from the target we calculate velocity v.

TOF is scintillator wall divided into eight modules and each module consist eight scintillator rods (this is for each of six sectors), i.e. in total there is 384 scintillators. On

both ends of these scintillators is photomultiplier (PMT) which allows us to calculate the position of hit from time difference

$$x = \frac{1}{2}\left(t_{\text{right}} - t_{\text{left}}\right) \cdot v_{\text{g}}, \tag{1.5}$$

where v_{g} is group velocity of light in the scintillator and t_{PMT} are times of photon registration in each PMT. The time resolution, that determine also the x spatial resolution (along the scintillator rod), is $\sigma_t = 190\,\text{ps}$, i.e. for spacial resolution $\sigma_x \approx 2.5\,\text{cm}$ (from tests we get the group velocity $v_{\text{g}} = (15.4 \pm 0.2)\,\text{cm/ns}$ [9]). In the other two coordinates the spatial resolution is determined by the cross-section of the rod which is $3 \times 3\,\text{cm}^2$ for the 192 outermost rods and $2 \times 2\,\text{cm}^2$ for the 192 inner ones. Also the length L of the scintillators differs from 1 m up to 2 m. The time-of-flight t is calculated as

$$t = \frac{1}{2}\left(t_{\text{right}} + t_{\text{left}} - \frac{L}{v_{\text{g}}}\right) - t_0, \tag{1.6}$$

where t_0 is time measured by START detector. One can also gain an information about energy losses of a particle in scintillator that might be useful in the particle identification process (but it is not as important as the time separation of different particles)

$$\Delta E = k\sqrt{a_{\text{right}} \cdot a_{\text{left}} \cdot e^{-L/\lambda_{\text{att}}}}, \tag{1.7}$$

where a_{PMT} are the amplitudes of PMT signals, λ_{att} is attenuation length of light in the scintillator and k is constant. TOF covers space with polar angle $44° < \theta < 88°$ and whole azimuth angle. The detector is shown on figure 1.9.

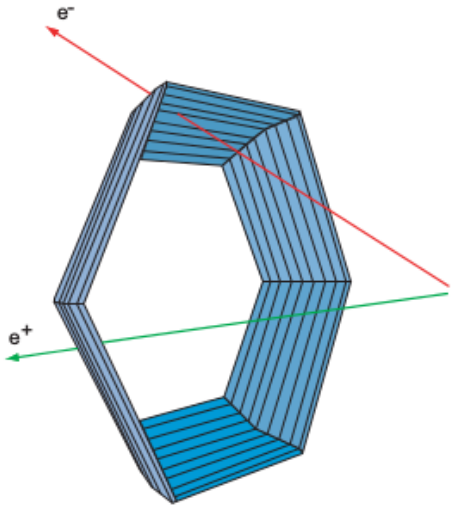

Figure 1.9: Scheme layout of TOF detector with example of registration electron and positron. Taken from [7].

1.7 Resistive Plate Chambers

As mentioned above second detector for measuring the stopping time in time of flight are Resistive Plate Chambers (RPC). This technique for registering particles is rather new, first RPCs were used in 1980's [10]. In principal passing particles ionise the gas between two electrodes covered by high resistance plate. Originally these plates were made of a phenolic resin (Bakelite) but nowadays they are usually made from soda-line glass which is very commonly produced (its volume resistivity is $\rho \approx 10^{12}\,\Omega\mathrm{m}$). There are two types of operational mode of RPCs:

- streamer mode - register stream of charges thanks to high secondary ionisation (used for triggering),
- avalanche mode - register the charge of electrons and ions in avalanche (used in timing RPCs).

Typical gas mixture is 85 % of $C_2H_2F_4$, 10 % of SF_6 and 5 % of $\mathrm{iso} - C_4H_{10}$. Each gas has some purpose: in $C_2H_2F_4$ the electron-avalanche is well propageted, SF_6 extend so called streamer-free zone and $\mathrm{iso} - C_4H_{10}$ is UV quencher.

In order to improve properties of RPC detectors the multigap design was developed. Between two metal electrodes with big electric potential difference is places glass plate as electrically floating electrode. The improvement is in detection efficiency

$$\varepsilon_N = 1 - (1 - \varepsilon_1)^N\,, \tag{1.8}$$

where ε_i is detection efficiency of RPC with i gas gaps and N is number of gaps. Also the time resolution σ is improved

$$\sigma_N = \frac{\sigma_1}{\sqrt{N}}. \tag{1.9}$$

RPCs used in HADES setup have 4 gas gaps (that are very thin - 270 μm) divided by 2 glass and 3 aluminium electrodes all with 2 mm thickness, see figure 1.10. The gas mixture used is a little bit different (90 % of $C_2H_2F_4$ and 10 % of SF_6). Nominal high voltage on aluminium electrodes is 5.5 kV. This detector covers area of 8 m^2 in polar angle $12^\circ < \theta < 45^\circ$ and almost full azimuth angle. Because of the expecting high rates and multiplicities of detecting particles (up to 1 $\mathrm{kHz/cm}^2$) and required detection efficincy and maximal occupancy of one RPC chamber the detector is divided into 1116 cells. Each from 6 sectors has 2 layers of cells in 3 columns where each one has 31 cells ($6 \cdot 2 \cdot 3 \cdot 31 = 1116$), see figure 1.11. Experimental time resolution is $\sigma_t = 60$ ps.

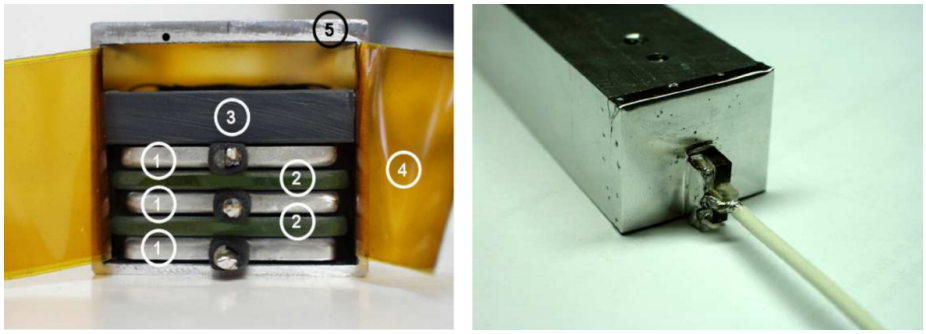

Figure 1.10: Internal layout of one RPC cell. On the left picture: 1 - Al electrodes, 2 - glass electrodes, 3 - pressure plate, 4 - kapton insulation and 5 - Al shielding. Taken from [10].

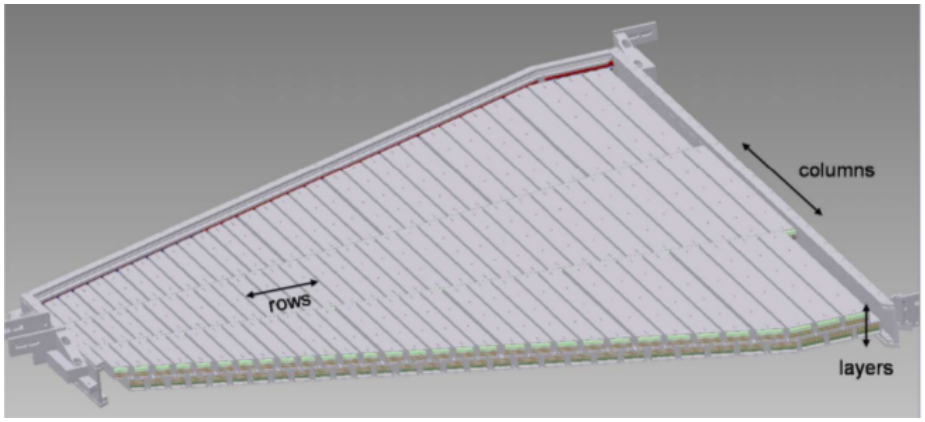

Figure 1.11: Cell distribution of one RPC sector. Taken from [10].

1.8 Shower detector

Another detector that shall clearly distinguish electrons from hadrons is Shower[1] [2]. It covers the region for polar angle $18° < \theta < 45°$ and full azimuth angle (it is also divided into six sectors and so between them is small dead area). From the position of Shower detector one can deduce that it will detect particles with large momentum which also means large energy ($E \gg 10\,\mathrm{MeV}$). In this interval of energy electrons tend to create electromagnetic showers during interactions with matter and their identification with only time-of-flight detectors is not easy because of very fast pions presence. The cross-section of Shower detector is shown on figure 1.12.

Physics background of electron identification in the Shower detector is based on detecting electromagnetic shower if electron pass through while probability that hadrons (for

[1]For the future beam times on FAIR facility, Shower should be replaced by electromagnetic calorimeter which is currently under development [11].

example on the Shower scheme 1.12 is displayed proton) will create hadronic shower is kept low thanks to adjusted thickness of lead plates (their thickness is 1.2 cm what corresponds to the radiation length $^{X}/_{X_0} \approx 2$). Prospective hadronic shower is narrower than electromagnetic shower which enables the identification of type of passing particle. Particles going through Shower are detected in the wire chambers (two types of wires are included: grounded field wires with 125 μm in diameter and potential wires with high-voltage up to 3500 V and thickness of 25 μm) filled with isobutan-based gas mixture. These chambers are operating in so called self-quenching streamer mode which advantage is in independence of collected charge on specific particle losses and though the charge is correlate to the number of particles passing through the chamber. In order to achieve good granularity the read out plain in divided into 942 pads which area is chosen so that their geometrical acceptance is the same with respect to the target position. The electron recognition algorithm than just compare multiplicity in one hitted pad plus eight surrounding ones in pre-chamber with its corresponding nine pads in post1 and post2 chamber and if the number of hits is rising (according to function that was determined from simulations) then the particle was electron.

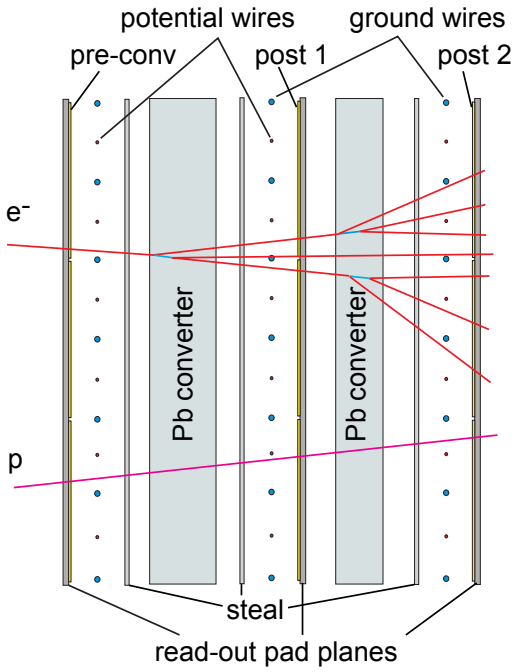

Figure 1.12: Cross-section of Shower detector. Taken from [7].

1.9 Forward Wall

The complete name of detector is Forward hodoscope Wall (FW) and it describe the functionality of the detector very well. Usually FW is placed 7 m behind the target and so it covers polar angles $0.33° < \theta < 7.17°$ but the support structure on wheels permits to move it anywhere. It is made from plastic scintillators divided into 140 small cells ($4 \times 4\,\mathrm{cm}^2$), 64 middle cells ($8 \times 8\,\mathrm{cm}^2$) and 84 big cells ($16 \times 16\,\mathrm{cm}^2$) [12]. Each cell has its own photomultiplier for read out the signals. The granularity is chosen so the dimension of cells is growing with the growing distance from the beam spot, see figure 1.13. This detector should measure the orientation of reaction-plane in azimuth angle and enables to study elliptic flow. For that it registers spectator nucleons and fragments emitted from the heavy-ion reaction in the target. The experimental time resolution is $\sigma_t = 500\,\mathrm{ps} \Rightarrow \sigma_p/p = 11\,\%$ and the angular resolution $\sigma_\phi \approx 45°$.

1.10 Data Acquisition System

Reading out all information from already mentioned detectors is job of **D**ata **A**c**Q**uisition system (DAQ). In total the DAQ must transfer information from 30 000 time-to-digital converters (TDCs) and 50 000 analogue-to-digital converters (ADCs) [13]. The data transfer is asynchronous due to different speed of response and different dead times from the detectors. System can handle without problem event rate of few tens kHz (up to peak 50 kHz) and typical data rate 300 MB/s. Signals from detectors first goes to Front-End Electronics (FEE boards) which usually contain some TDCs and ADCs than the information is processed in Read Out boards (in most cases Trigger and Read out Boards - TRB) and through the network infrastructure is sent to Central Trigger System (CTS) or to Slow Control System for online monitoring during data taking or finally to Event Builders (EB) that takes the correct information together and store them on server discs and tapes. The correct running of the system is controlled by 550 Field Programmable Gate Arrays (FPGAs) that are integrated circuits which can be programmed to provide any logical function. The overview of the DAQ system in shown on figure 1.14. The boards connects 7 km of optical cables to cope with this very high event and data rate.

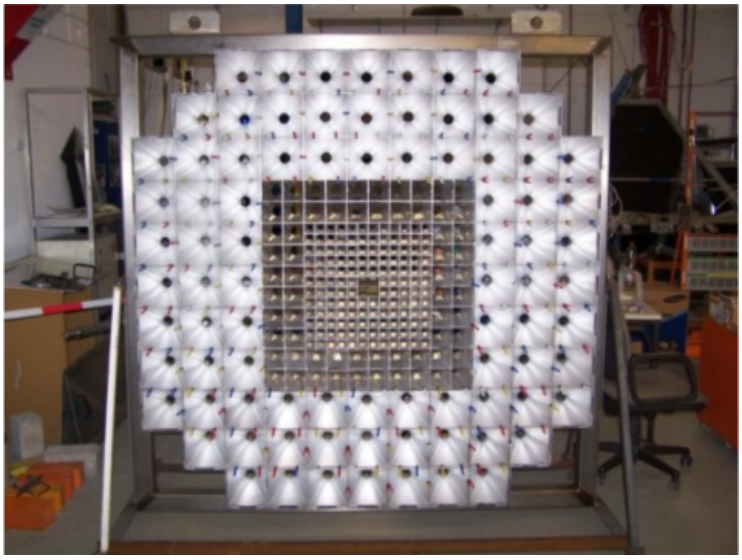

Figure 1.13: The photo of uncovered Forward Wall. During measurement the is a black foil over whole detector to reduce number of photons from background. Taken from [3].

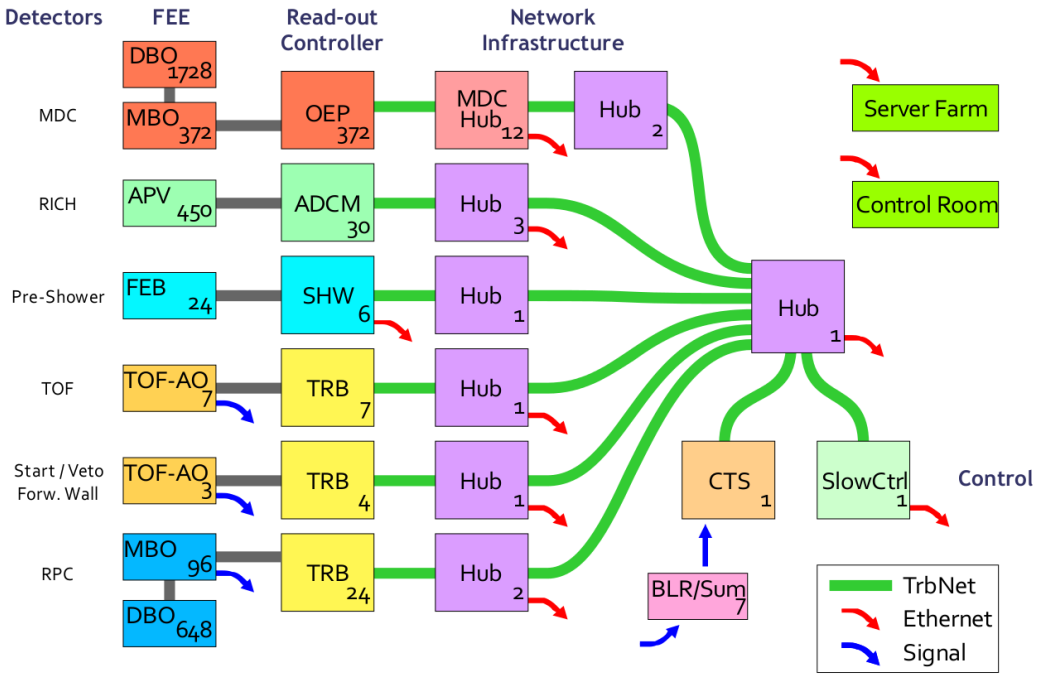

Figure 1.14: DAQ system layout. Taken from [13].

CHAPTER 2

Hodoscope for π^- beam

Hodoscopes are used in the particle physics for detection of the charged beam particles and to determine their trajectories. The hodoscopes are usually consisted of scintillators and photomultipliers (PMTs). One can distinguish between different particles based on measuring the time of flight and calculating the trajectory in known magnetic fields. Sometimes might be also helpful the information about the deposited energy in the scintillator material. The time resolution is influenced by the group velocity of light in the scintillator, intrinsic time resolution of the PMT and the read out electronics. The position resolution is influenced by the partition of the scintillator into smaller independent parts.

The hodoscopes we used were originally made for another pion beam experiment in 2000 [14]. They were used in the pion beam line for separation different particles because the pion beam is a secondary beam. It means that from accelerator flights protons or ions (like ^{12}C, ^{14}N) and they collide with so called production target made from beryllium. Production target is very thick ($18.4\,\mathrm{g/cm^2} \sim 10\,\mathrm{cm}$ length) to stop primary beam inside and from the interactions we get secondary beam that contains predominantly pions, protons and fragments from original target nucleus like deuterons (partially there might be also electrons, muons and kaons). Particles with narrow momentum spread are selected with bending dipole magnet on the 33 m long beam line. However final pion discrimination is possible only with measuring t_{tof} the time of flight between two hodoscopes and using the equation

$$mc^2 = \frac{pc}{l}\sqrt{(ct_{\mathrm{tof}})^2 - l^2}, \tag{2.1}$$

where l is the trajectory length between hodoscopes, m the rest mass of particle and p is the beam momentum.

For the recent pion beam (held in GSI during summer 2014) new system of beam line detectors was developed. To determine momenta of each secondary pion interacting in target two silicon based detectors in combination with START diamond detector were

used [15]. This pion beam detector called Pion Tracker[1] has better position resolution than hodoscopes that enables very accurate momentum reconstruction. We prepared two hodoscopes (one as a spare) labelled as H1 and H2 in [14] as the second part of beam line detector system. One of these hodoscopes was used to monitor secondary pion beam behind HADES setup, see figure 2.1.Both hodoscopes have 16 rods made from plastic scintillator BC404. Every rod is 10 cm long, 1 cm wide and 5 mm thick and it is wrapped in 40 μm aluminium plated Mylar foil. At both ends of the scintillator are glued light guides which pass the light signal to PMTs Hamamatsu R3478, for better notion see schemes on figures 2.2 and 2.3.

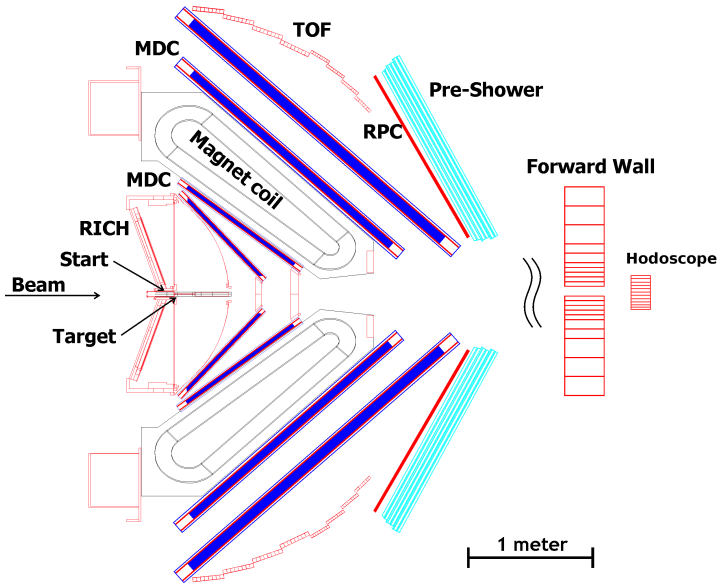

Figure 2.1: The cross section of HADES setup used during the pion beam experiment. Taken from [3].

2.1 Testing of hodoscopes

The hodoscopes were transported from GSI to Nuclear Physics Institute of the ASCR in Řež (in next NPI) in autumn 2013. They were not used for a very long time so our first task was to test the functionality. As a high voltage power supply for Hamamatsu PMTs (nominal HV is 1500 V) we used CAEN SY4527. For digital visualisation of measured scintillation signals we had Tektronix TDS 3052 oscilloscope. Because of the simplicity of this test we measured charged particles in the cosmic rays. Immediately we saw that several PMTs are not working because we could see signals from one side of the scintillator rod but not from the other side. Reason for this we found out after dismounting one face of

[1]START detector and Pion Tracker formed together **Ce**ntr**a**l **Be**am T**r**acker for Pi**o**n**s**. The abbreviation is CERBEROS for the three headed hell-hound from Greek mythology that guarded Underworld where the god Hades ruled.

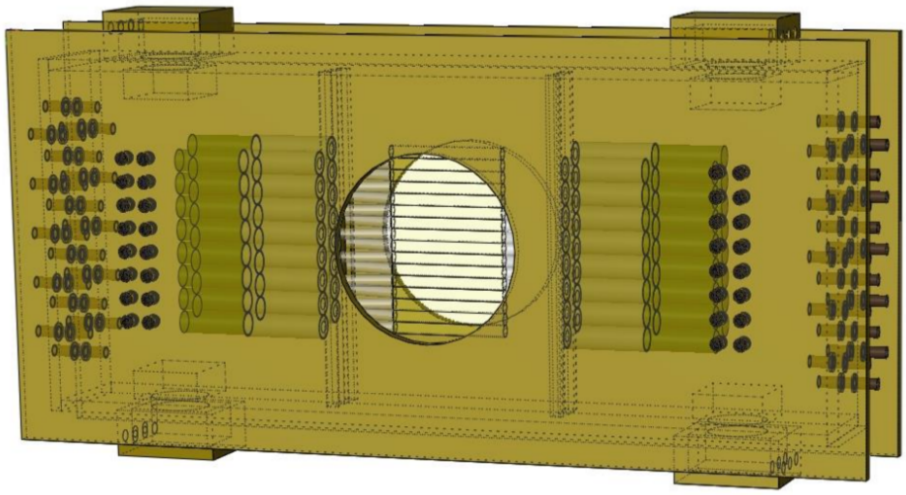

Figure 2.2: Complete technical scheme of the hodoscope. Prepared by O. Svoboda using SimpleGeo program.

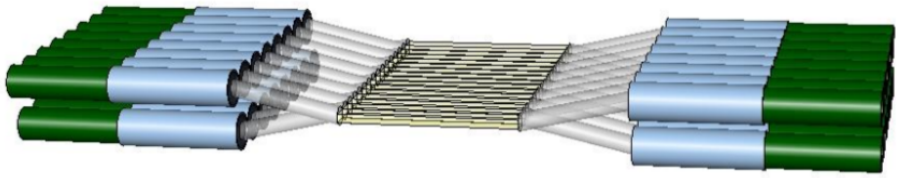

Figure 2.3: Technical scheme of the inner part of the hodoscope. Prepared by O. Svoboda using SimpleGeo program.

the black metacrilate box that houses the hodoscope, few PMTs were no longer connected to the light guides probably due to careless handling, see figure 2.4.

Figure 2.4: Photo of the hodoscope after removing one face of the box.

Before sending the hodoscopes to Optical Laboratory of Faculty of Mathematics and Physics of Charles University in Prague for repair we performed several tests of the attenuation length of scintillator rods. The attenuation length l_{att} is defined as length of a material where the intensity of light will decrease on $1/e$ of the original value. Light intensity as a function of distance x that light travels through a material can be described by relation

$$I(x) = I_0 \exp\left(-\frac{x}{l_{\text{att}}}\right). \tag{2.2}$$

One gets the l_{att} from fitting experimental signal amplitudes from PMTs $A_{\text{PMT side}}$ measured for at least 2 places on the scintillator where the particles go through. From linear dependence

$$\left[\ln\left(\frac{A_{\text{right}}}{A_{\text{left}}}\right)\right](x) = \frac{2}{l_{\text{att}}} \cdot x + \ln\left(\frac{\text{yield}_{\text{right}}}{\text{yield}_{\text{left}}}\right) \tag{2.3}$$

it is possible to find out the value of l_{att} because

$$A_{\mathrm{right}} \sim \mathrm{yield}_{\mathrm{right}} \cdot I_0 \exp\left(-\frac{\frac{d}{2}+x}{l_{\mathrm{att}}}\right) \qquad A_{\mathrm{left}} \sim \mathrm{yield}_{\mathrm{left}} \cdot I_0 \exp\left(-\frac{\frac{d}{2}-x}{l_{\mathrm{att}}}\right), \tag{2.4}$$

where d is length of the scintillator rod. We decided to measure in three different positions of the rod: in the middle (thanks to this measurement we can compare the yields of the PMTs) and 1 cm from the ends.

As a source of particles we tried to use γ-sources (in particular ^{241}Am and ^{154}Eu) because of much higher event frequency that with cosmic rays. The disadvantage of γ-source is in less opportunity to ensure the position of energy deposition in scintillator. We tried to put the sources directly on the scintillator but even with a point like approximation of the source there is a certain probability that the photon emitted from source will interact for example in the middle of the rod. To decrease this probability we built a lead shielding around the γ-sources. Applying the averaging of pulses with Tektronix oscilloscope, see figures 2.5 and fitting the averaged pulse high, figure 2.6, we got the attenuation length for 2 rods: $l_{\mathrm{att}}^{\mathrm{rod\#2}} = 3.8\,\mathrm{cm}$ and $l_{\mathrm{att}}^{\mathrm{rod\#4}} = 5.4\,\mathrm{cm}$.

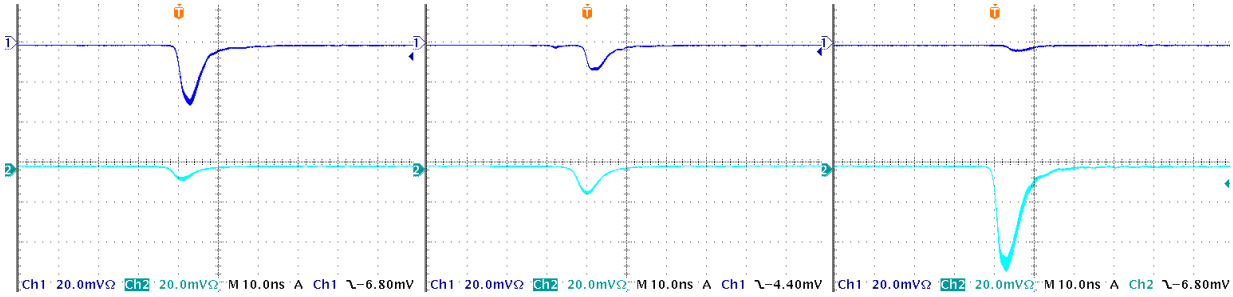

Figure 2.5: Pictures of averaged pulses from oscilloscope. Channel 1 (dark blue) is left PMT and channel 2 (turquoise) is right PMT. The picture on the left side corresponds with left position of the source (1 cm from left edge of scintillator rod), the middle picture is from measurement with source in the centre of the rod and right picture is for source 1 cm from right edge of scintillator rod.

To improve the measurement we asked our colleague V. Mikhaylov for writing simple data acquisition in LabVIEW program for measuring the amplitude of signals coming out of the PMTs and processed with 8-channel digitizer oscilloscope National Instruments PXI-5105. Due to uncertainty in position of photon interaction with scintillator we chose to use cosmic rays again. The position of passing particle we selected with two external scintillators (both with proportions $1 \times 1 \times 3\,\mathrm{cm}^3$, one placed below and second above the hodoscope) and read out by PMTs. The coincidence of signals from these PMTs was used as a trigger for the measurement with the hodoscope's PMTs. The only disadvantage of this method is the time consumption because of very small geometrical acceptance (the event rate was 1 event/h). As a result of the measurement with cosmic rays we got the attenuation length for two neighbours rods $l_{\mathrm{att}}^{\mathrm{rod\#15}} = 7.1\,\mathrm{cm}$ and $l_{\mathrm{att}}^{\mathrm{rod\#16}} = 13.8\,\mathrm{cm}$, see

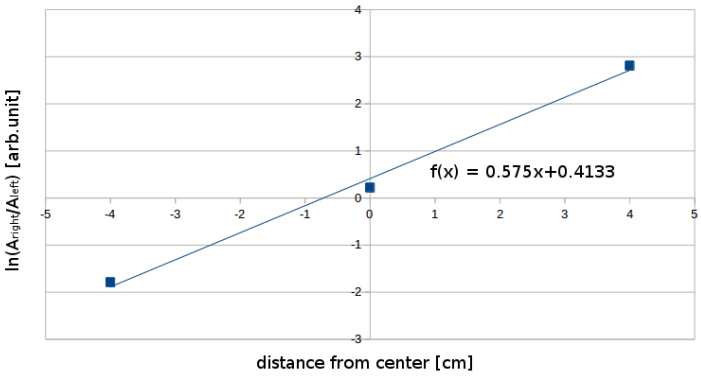

Figure 2.6: Linear fit of $\ln\left(A_{\text{right}}/A_{\text{left}}\right)$ on distance x from the centre of hodoscope's rod.

figures 2.7 and 2.8. According to Bicron official data-sheet for the plastic scintillators the attenuation length for BC404 is 140 cm but it is measured for dimensions of the scintillator $1 \times 20 \times 200\,\text{cm}^3$ which is very different from the dimension of rods used in the hodoscopes. The difference in dimensions can have an influence on attenuation length [9]. Unfortunately there was no reference measurement of the attenuation length in year 2000 when the hodoscopes were made but it was decided to exchange the scintillator as a part of repair done in Optical Laboratory.

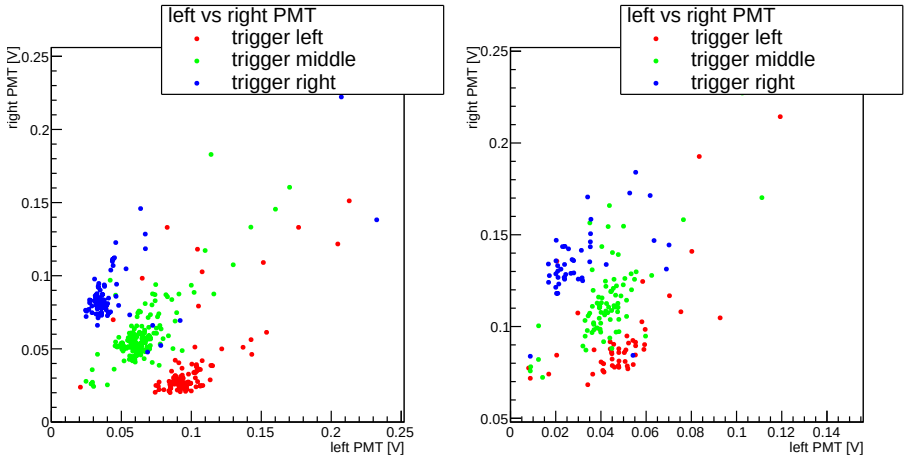

Figure 2.7: Measured amplitudes from left/right PMTs for 3 different small scintillators (trigger) position. Left picture is for rod #15 and right for rod #16.

After the repair there were only 14 days before we had to transport one of the hodoscopes back to GSI for the proton beam test (more details about this topic is in 2.2). Thus we could only test the functionality of all channels with cosmic rays and Tektronix oscilloscope. However we also noticed that the differences between the signal amplitudes for one rod are more similar than it used to be so it looked like the problem with short

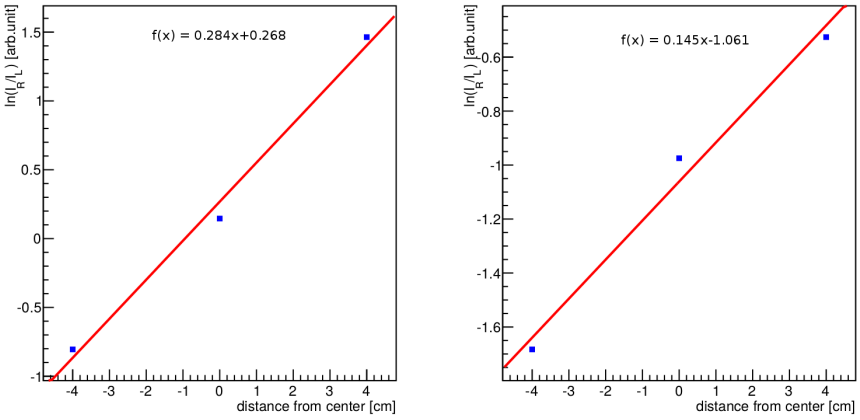

Figure 2.8: Linear fit of $\ln\left(A_{\text{right}}/A_{\text{left}}\right)$ on distance x from the centre of hodoscope's rod. Left picture is for rod #15 and right for rod #16.

attenuation length is solved too. In GSI we had few more days before the proton beam test of beam-line detectors so we tried to measure the attenuation length again. This time we used ^{90}Sr β-source and as a data acquisition we used modern Rohde&Schwarz RTO 1044 oscilloscope. To ensure the position of passing electrons through the hodoscope we had one addition small scintillator placed beneath the hodoscope and we put the β-source directly on top of the scintillator rods. The results of the measurement one can see on figure 2.9 and the attenuation length was $l_{\text{att}} \approx 24\,\text{cm}$.

We also transferred the second hodoscope to GSI as a back up solution for the upcoming pion beam. We did also the attenuation length measurement with β-source in GSI with following result: $l_{\text{att}}^{\text{rod\#8}} = 8.9\,\text{cm}$ and $l_{\text{att}}^{\text{rod\#9}} = 9.5\,\text{cm}$, see figures 2.9 and 2.10.

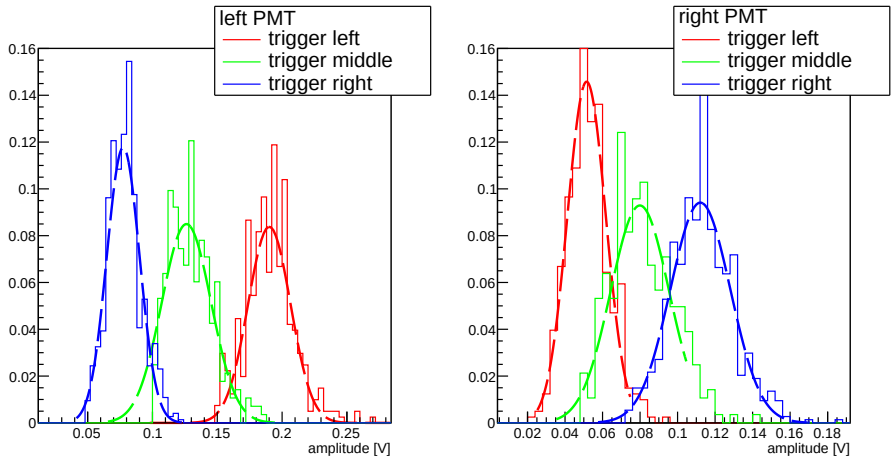

Figure 2.9: Normalised and fitted histograms of signal amplitudes for different β-source (trigger) position and both PMTs from rod #9. Mean amplitudes are then used in calculations.

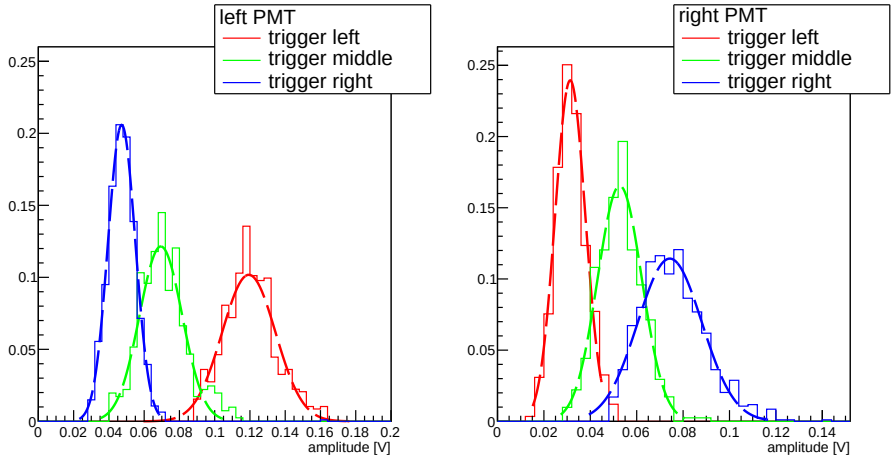

Figure 2.10: Normalised and fitted histograms of signal amplitudes for different β-source (trigger) position and both PMTs from rod #8. Mean amplitudes are then used in calculations.

2.2 Proton test beam

This test beam in May 2014 was supposed to prove the functionality of all beam line detectors (Pion Tracker, START detector and hodoscope) with minimum ionising particles (MIPs) because of the HADES π^- experiment planned to be held from June to September 2014, more details in 2.3 and 4. There was also in plan to make measurement for different beam momentum to determine several coefficients from transport model calculations. And afterwards find the best possible tuning of beam-line magnets for the pion beam.

The hodoscope was transported to HADES cave in GSI where it was mounted on specially prepared construction and placed behind HADES detector, see figure 2.11. We places the hodoscope as close to the HADES detector as possible. This position was chosen with respect to requirement on the resolution of hodoscope in y-direction. Even behind the hodoscope was placed Forward Wall (FW) detector. The need of another forward detector, in this case the hodoscope, is because the position resolution of FW is not good enough for testing the beam optics and beam monitoring detectors[2].

As readout electronics we used TRB3 (general purpose Trigger and Readout Board version 3) and as front-end electronics PaDiWa AMPS (version of PandaDircWasa board with amplifiers), both were developed in GSI. The PaDiWa boards are meant to be used for PANDA experiment at FAIR facility[3]. Their design is determined by "COME and KISS" rule which tells us to use **com**mercial **e**lements and **k**eep **i**t **s**mall and **s**imple. It lead to developing electronic board which can be simply adjusted to typical pulse shape

[2]Moreover the FW has in the middle hole with proportions 8 cm × 8 cm.

[3]The research program of PANDA experiment contains deep exploration of the weak and strong forces, exotic states of matter and the structure of hadrons. More information about this project can be found at `http://www-panda.gsi.de/`.

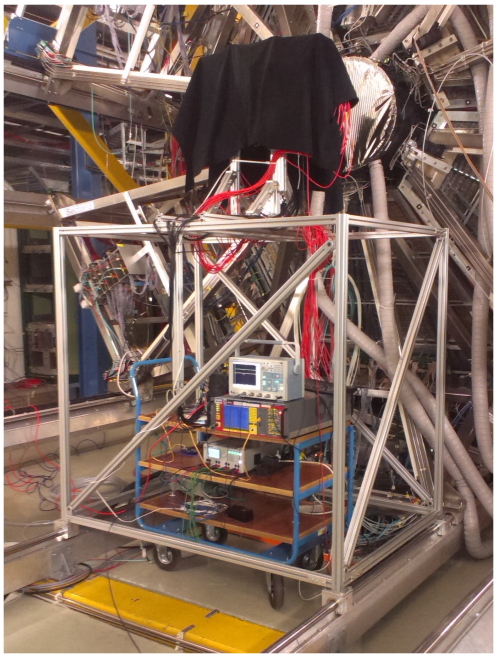

Figure 2.11: Position of the hodoscope in HADES cave.

by adding resistors and capacitors, see figure 2.12. To each PaDiWa board we connected 8 cables from 8 PMTs in the hodoscope and all four PaDiWas were connected to one TRB3. Main advantage of TRB3 is their compatibility with a lot of addons as one can see on figure 2.13. For our purpose we had one TRB3 with cable converter extension which is in lower left corner of figure 2.13. With this setup we were able to get the rising and falling time of pulses but not the amplitude. However it was no problem as the hodoscope was used in Central trigger System (CTS) for starting the data acquisition.[4]

First thing we did, after connecting the hodoscope to high-voltage source and readout electronics, was setting thresholds because we needed to cut off the electronic noise. After that we calibrated the response of the hodoscope in the way that we saw on oscilloscope: pulse with amplitude about 200 mV. As a source of ionising radiation we used again electrons from ^{90}Sr β-source. For adjusting the amplitudes we changed HV on the PMTs inside hodoscope. Small problem occurred on 2 PMTs where it was not possible to safely get the same amplitude size (probably due to ageing of PMTs) so we set the high voltage to the value which the producer denotes as maximal (1800 V).

Our colleagues from GSI have developed very nice on-line monitoring for the hodoscope so we could do real-time control of the response of the detector. We had to be careful with the intensity of the beam because if the intensity would be too high the current in PMTs would increase and it might damage the PMTs. In the on-line monitoring system one could

[4]Originally there was plan that the hodoscope would be used as a veto detector for diamond START detector. Unfortunately this diamond detector broke down during installation of copper target. The air gets into the vacuum tube and the shock wave damaged the detector.

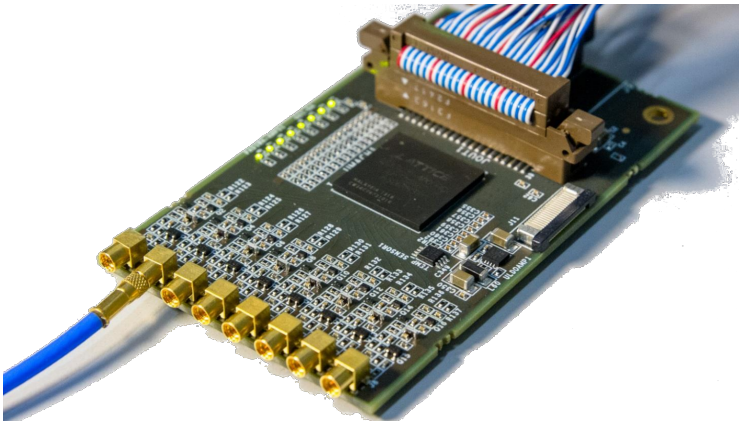

Figure 2.12: PaDiWa AMPS board. Taken from [3].

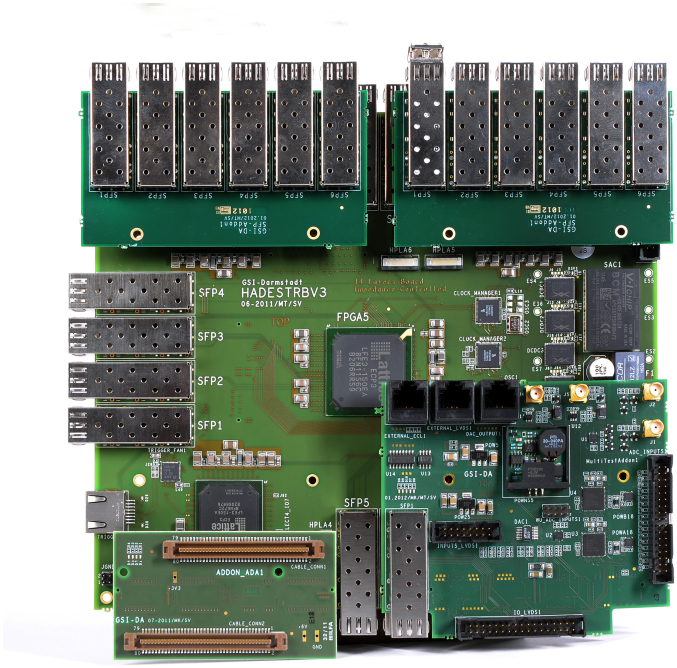

Figure 2.13: TRB3 board with different addons. Taken from [3].

see integrated number of pulses from each PMT, see figure 2.14.

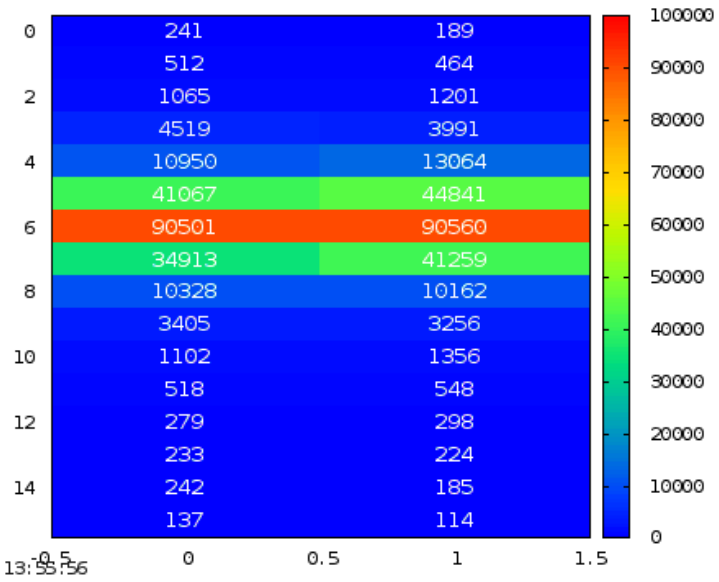

Figure 2.14: Picture from on-line monitoring system. Numbers in cells are sums of number of pulses from PMTs during one second. One can see the y-profile of proton beam.

During one day break in proton test beam we took data with cosmic radiation for 24 hours. The functionality of the hodoscope can be tested if one look on a number of hitted PMTs in one event. If the thresholds are set to the correct value then there should not be huge electronic noise and the number of hitted PMTs should be even (the odd number is due to electronic noise on one PMT plus two times the number of hitted scintillator rods). From figure 2.15 it is clear that the electronic noise reduction was working quite well.

Another topic of the analysis of the data taken with cosmic was the time resolution of the hodoscope. We studied the time differences between hits in two rods. Each hit in one rod has a time stamp that is determined by the same equation (1.6) as for TOF measurement thanks to the similar design of the detector. We had to eliminate the contribution of different path length between the two hits in the hodoscope using cut on the time difference from left and right PMT

$$|(t_{\text{left},1} - t_{\text{right},1}) - (t_{\text{left},2} - t_{\text{right},2})| < 50\,\text{ps}, \tag{2.5}$$

where the times are labelled as $t_{\text{PMT side,\#rod}}$ and the value 50 ps is chosen to cut the tails of time difference distributions but to still have enough hits for good statistics. The weighted average of the time resolution is $\sigma_t = 270\,\text{ps}$ where the weights are the fitted errors of σ of the Gaussian, see figure 2.16. However one has to keep in mind that this result is not perfect and the Hodoscope time resolution is probably better (in several combinations of the two rods the resolution was below 200 ps) because of the possible difference between hits position. In the following we will consider the value 270 ps as an upper limit for the time resolution of the Hodoscope.

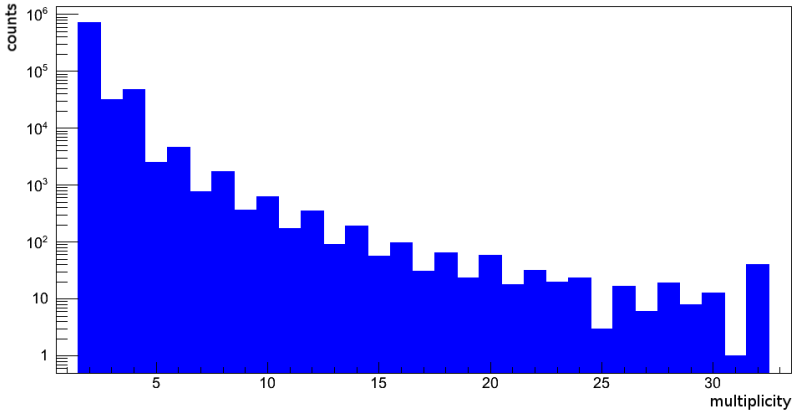

Figure 2.15: Spectrum of number of hitted PMTs in one event.

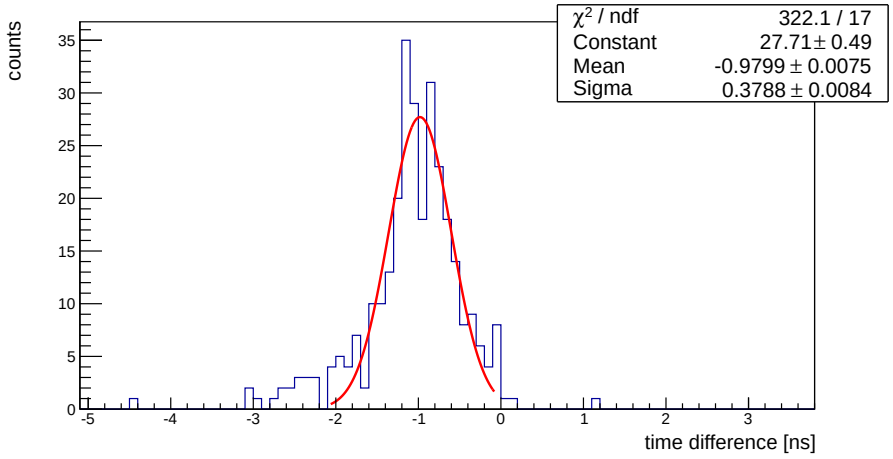

Figure 2.16: Example of the time difference between two hits in the hodoscope's rods. Around the fitted Gaussian peak we can see small noise contribution. Fitted parameter σ must be divided by $\sqrt{2}$ to get the hodoscope time resolution.

2.3 Pion beam results

After successful testing the Hodoscope was ready to be used during the HADES pion beam experiment. The main purpose of this detector was beam monitoring and during first days we also used it for time calibration of START detector (more about this is in section 3.1). The scheme of HADES beam line is shown on figure 2.17. The silicon strip detectors, called Pion Tracker with two stations each of them having two planes (one for x-direction and one for y-direction) with 128 strips on $10 \times 10\,\mathrm{cm}^2$, was used for the pion momentum determination. The diamond START detector, described in more detail in chapter 3, was used for the primary vertex reconstruction, t_0 measurement and for trigger.

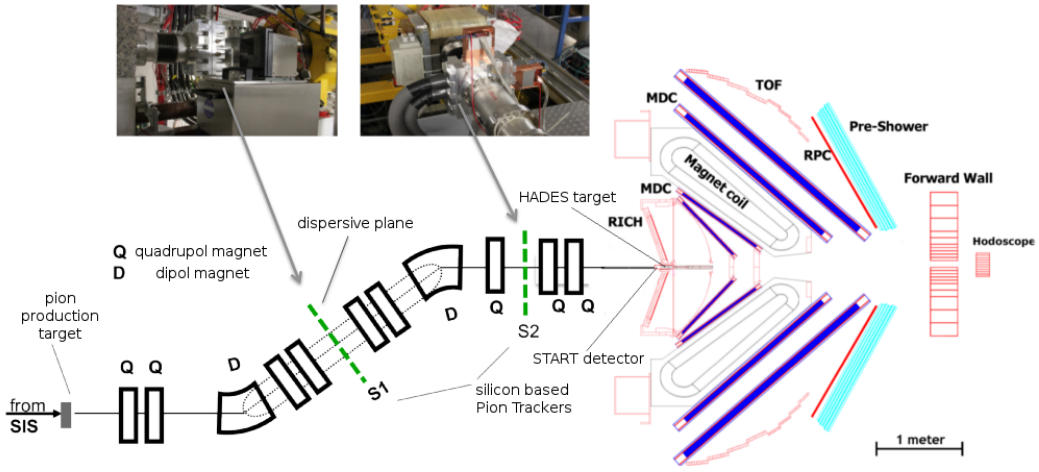

Figure 2.17: Scheme of pion beam line with all focusing magnets and beam detectors. Photos of Pion Trackers is included. Taken from presentation of Joana Wirth.

During the experiment the beam spot on the Hodoscope detector is on figure 2.18. The position of hit in y-direction is determined by the position of the hitted scintillator rod and in x-direction the time difference between both PMTs is used like in the case of TOF detector. However due to bad time resolution of the detector the uncertainty is large (several centimetres). The beam spot on both of Pion Tracker planes is shown on figure 2.19.

The question we asked ourselves was if we would see some correlation between the position of pion registered in the Hodoscope and other beam detectors. The reason why we wanted to examine this was that if we would find some correction we could try to measure the momentum of beam pions with the Hodoscope. However as one can see in figures 2.20 and 2.21 the position resolution is not that good for y-direction and in x-direction we do not see any correlation at all.

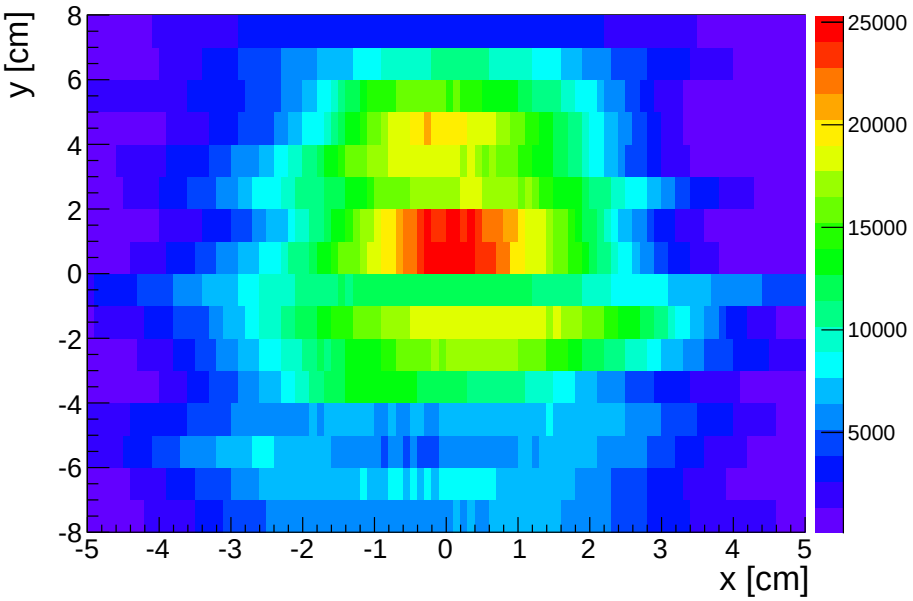

Figure 2.18: Beam spot at the Hodoscope.

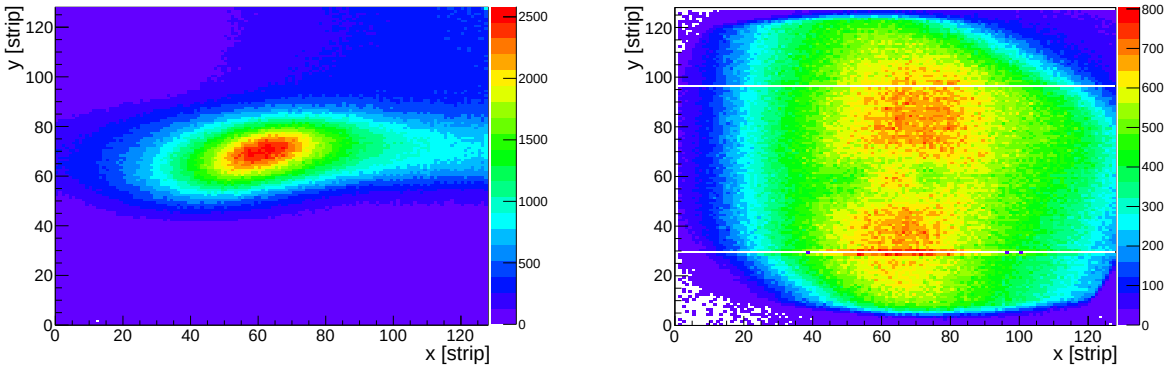

Figure 2.19: Beam spot at both Pion Tracker planes. On the left figure there is the beam spot on first Pion Tracker plane (counting from production target) and on the right is the second plane.

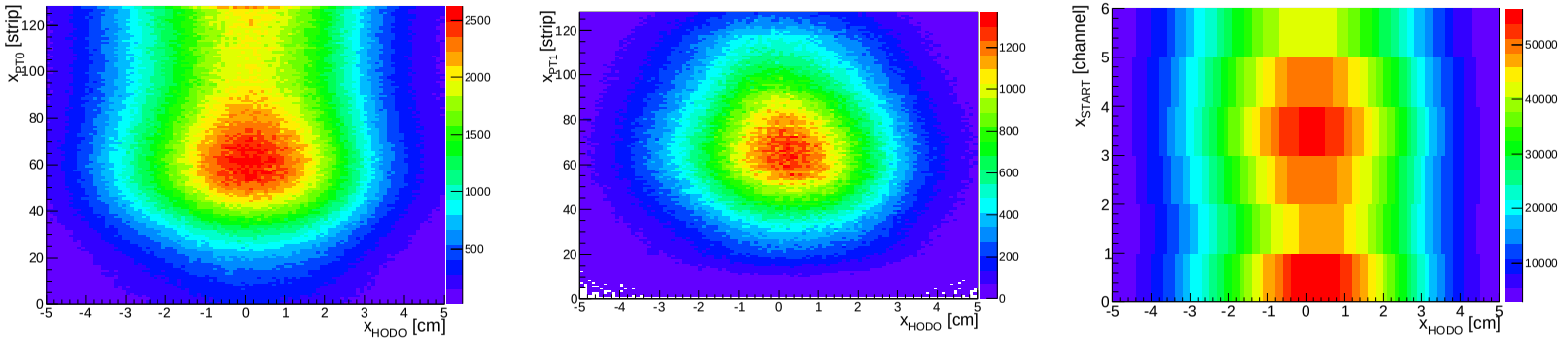

Figure 2.20: Correlation between the Hodoscope and other beam detectors in x-direction. On the left picture is correlation with first Pion Tracker plane, on the middle with the second plane and on the right picture with START detector.

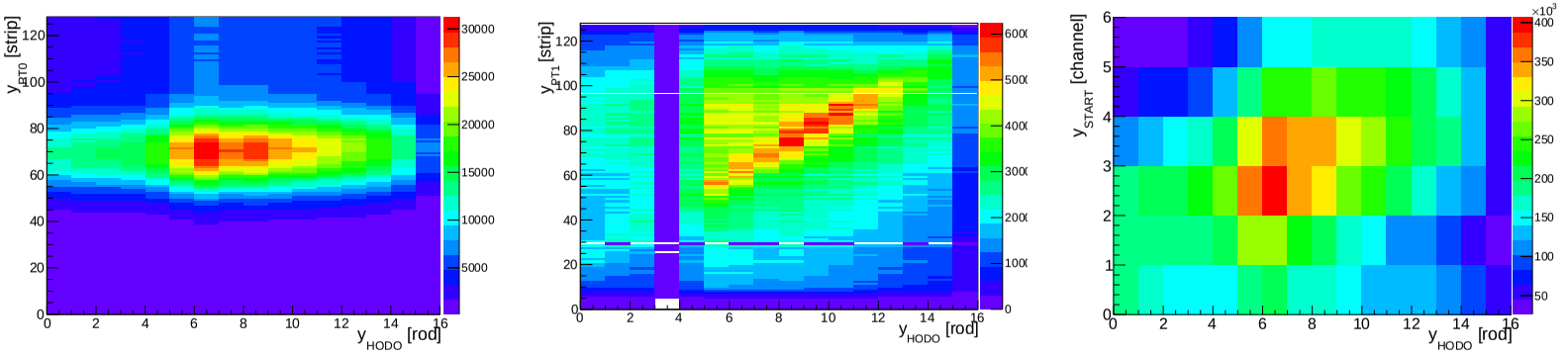

Figure 2.21: Correlation between the Hodoscope and other beam detectors in y-direction. On the left picture is correlation with first Pion Tracker plane, on the middle with the second plane and on the right picture with START detector.

CHAPTER 3

START Calibration and Time Resolution

Short and general description of the START detector was already mentioned in the section 1.2. Here will be only presented more details about one particular START detector which was used during the pion beam experiment. In the preparatory phase the design of the detector was studied and several requirements were put on the START detector:

- time resolution better than 100 ps,
- position resolution approximately 2 mm,
- high detection efficiency,
- high rate capability.

The START detector for pion beam experiment was made from 9 mono-crystalline CVD diamonds and the dimensions of each one diamond are: the area of $4.6 \times 4.6\,\mathrm{mm}^2$ and the thickness is $300\,\mu$m. That means in total the START detector covers almost $2\,\mathrm{cm}^2$. To satisfy the requirement on position resolution each diamond was segmented into 4 independent channels by surface metallization, see figure 3.1. This setup was chosen with respect to the area of cross-section of the used targets and the diameter of the beam (because the pion beam is secondary beam its transverse dimensions are much bigger that of the primary beam). Also the thickness of the detector was carefully chosen. Due to small energy losses of pions in diamond (pions with the momentum bigger than 200 MeV/c are in minimal ionising region) the thickness of the diamond must be bigger compare with the diamond detectors used for heavy ions. To create one electron-hole pair in diamond the passing particle must lose 13 eV and it means that MIP particle in $300\,\mu$m thick diamond creates only 14 000 pairs [4]. To register such a small signal the state-of-the-art electronics must be used. Due to small signal amplitude the first stage signal amplification has to be done as close as possible, i.e. directly on the PCB boards. Because of the limited space on

the boards one of the smallest amplifiers were developed. Outside of the beam pipe there was second stage amplifiers and after them there were NINO boards that discriminates the signals. At the end there is a TRB3 board that provides time measurement and communication with the DAQ system.

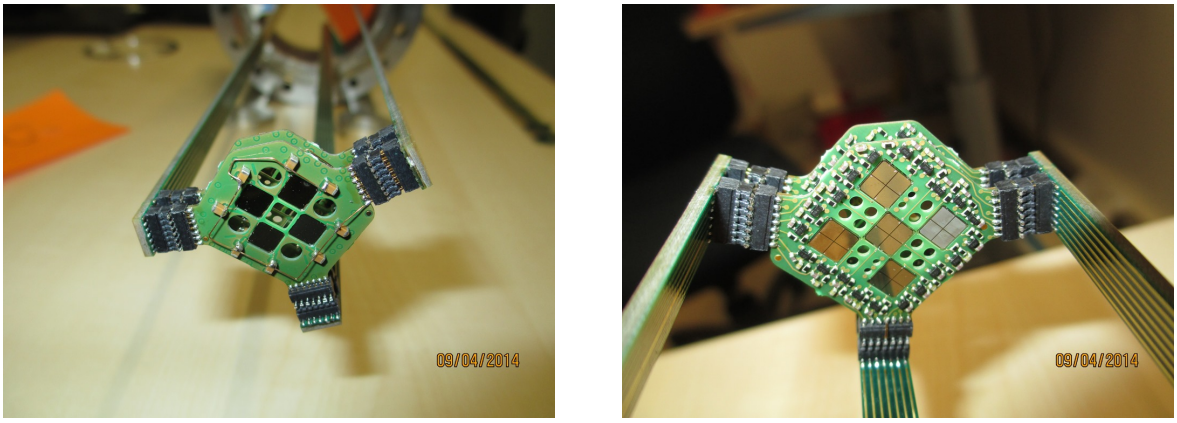

Figure 3.1: Photos of one PCB boards from the START detector with 4 and 5 diamonds. Kindly provided by Jerzy Pietraszko.

The time calibration of the START detector is crucial for the data analysis. The key is in splitting the signal from START to the trigger and data acquisition. As one can see on figure 1.14 there are blue arrows coming out of the FEE boards of START, TOF and RPC detector. These arrows represent direct connection from these detectors to CTS where the experts set the time delays between the signals from different detectors to get overlap coincidence that will start the data acquisition. In the data acquisition there is specific time window for each detector in which anything will happened will be stored in files. However inside these files we need to know the relation between for example the time stamp from the TOF detector and time stamp from the START detector and the procedure to find the relation is called calibration.

In very short way one can say that we just made time difference between two detectors and by shifting the mean value of the distribution we calibrate the detectors and from the width of the distribution of the time difference we also find the time resolution. I will try to describe the procedure in more details in following sections 3.1, 3.2 where the two methods we used during the data taking are described.

3.1 Using pions

The first of the two methods made is exploiting pions that did not interact with the target and they continued flying straight, uninfluenced by the magnetic field of the HADES magnet. The Hodoscope was placed at a distance of 5.7 m from the START detector to detect non-interacting pions (the interaction probability in the target was less than 5%). The problem that must be addressed is that the DAQ trigger was defined by the overlap

coincidence of the signal from the START detector and that from TOF or RPC. This condition only separates events in which some pion from the beam interact with nuclei in the target. Fortunately, there is a 2 μs time window set around the trigger signal, when the signals from detectors are also stored in output data files. In figure 3.2 the time spectrum for both detectors is shown. Apart from the trigger peak there is visible the micro-bunch structure of the secondary pion beam that was used to connect hits in the START and the Hodoscope detectors. For the purposes of this analysis we used all hits in the START detector and the Hodoscope with times out of the trigger peak.

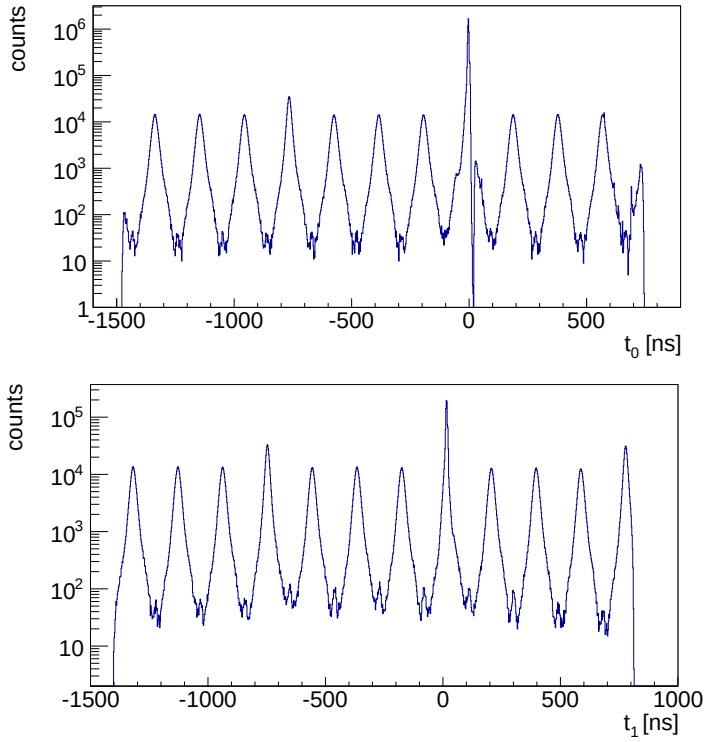

Figure 3.2: Time spectrum with trigger peak at 0 ns from the START detector (upper figure) and from the Hodoscope detector (lower figure). Note the logarithmic scale on the y-axis.

By subtracting measured time t_0 at the START and time t_1 at the Hodoscope for each pion the distribution that is shown in figure 3.3 is obtained. It is clear that from the σ of this Gauss-like distribution, only the combined resolution of the detectors ($\sigma^2 = \sigma^2_{\mathrm{START}} + \sigma^2_{\mathrm{Hodo}}$) can be deduced. Since neither σ_{START} nor σ_{Hodo} is known separately[1], the assumption

$$\sigma_{\mathrm{START}} = \sigma_{\mathrm{Hodo}} = \frac{\sigma}{\sqrt{2}} \tag{3.1}$$

was made and this results to $\sigma_{\mathrm{START}} = 283\,\mathrm{ps}$. We made the subtraction $t_1 - t_0$ for each START channel and each Hodoscope rod. Because there were 4 independent channels per

[1] In section 2.2 was mentioned that the time resolution of the Hodoscope is better than 270 ps, probably around 200 ps. These results were obtained from measurement with cosmic rays.

each diamond and 16 Hodoscope rods so in total we had 576 Gauss-like distributions. By shifting the mean of the distributions to value 19 ns (that corresponds to the time of flight of the particle with $\beta \approx 1$, which is true for the pions with momentum $p > 600\,\mathrm{MeV/c}$, on distance 5.7 m) we had calibrated the START detector and the Hodoscope. What one has to think about in this point is the accuracy of this calibration, i.e. we will focus now on the time resolution.

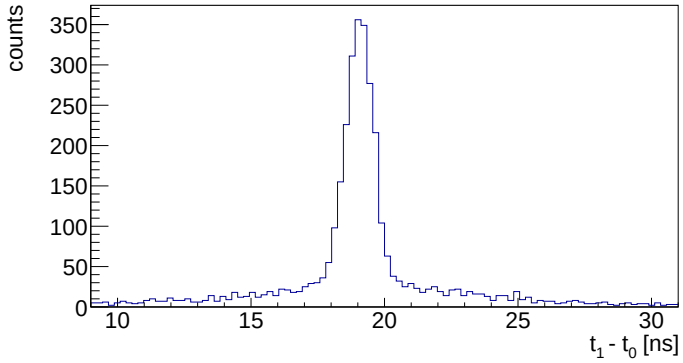

Figure 3.3: Distribution of time of flight for pions from the START detector to the Hodoscope.

For subtracting $t_1 - t_0$ the averaged time $t_1 = \frac{1}{2}(t_{\mathrm{left}} + t_{\mathrm{right}})$ is used. Beside the time measurement, there is also measurement of the amplitude of the pulses using the information from the width of the pulse. The amplitude of the signal is proportional to the amount of light that reaches the PMT and therefore depends on the length through which the light must travel inside the scintillator (because of the attenuation of the light in a material). When the dependence of time difference $t_{\mathrm{left}} - t_{\mathrm{right}}$ on the width of pulses measured by the photomultipliers is observed (see figure 3.4), it is possible to improve the result of σ of the time difference $t_1 - t_0$ distribution by selecting positions where the pions pass through Hodoscope's scintillators (this is proportional to $t_{\mathrm{left}} - t_{\mathrm{right}}$). For the selection we used cut on the difference $t_{\mathrm{left}} - t_{\mathrm{right}} \in (-0.3; +0.3)\,\mathrm{ns}$.

Another improvement can be made using so called time-walk corrections (or zero time correction). This means that from dependence of $t_1 - t_0$ on the width of the pulses, i.e. on the amplitudes of the pulses, measured by the START detector (see figure 3.5), the time difference is transformed in such a way that it will be independent of the width. The idea behind time-walk correction is that the pulses are sent to the leading edge discriminators, which have set threshold values that must be reached in order for the information proceed, see figure 3.6. Ideally measurements should be made from a zero value but this cannot be done efficiently owing to electronic noise. The time, that the pulse needs to cross over the threshold value, depends on the energy of the registered particle which is unwanted. Applying these two procedures results in a time resolution for the START detector (and also the Hodoscope, see equation (3.1)) of $\sigma_{\mathrm{START}} = 173\,\mathrm{ps}$. Since the objective is a resolution $< 100\,\mathrm{ps}$ this result is not positive. It is also important to note that this resolution is just an estimate, since the contribution of the Hodoscope to the total time resolution σ is unknown.

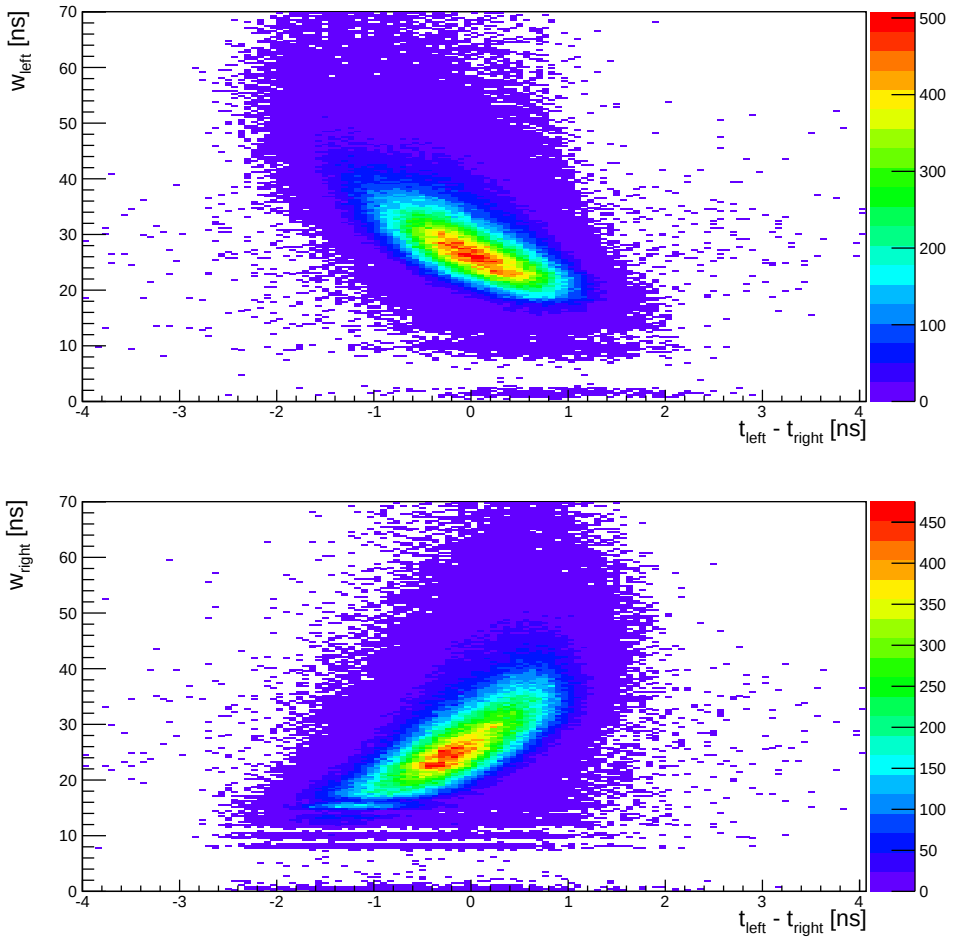

Figure 3.4: Dependence of the width of the pulses from left or right photomultiplier of the Hodoscope (w_{left} or w_{right}) on time difference $t_{\mathrm{left}} - t_{\mathrm{right}}$.

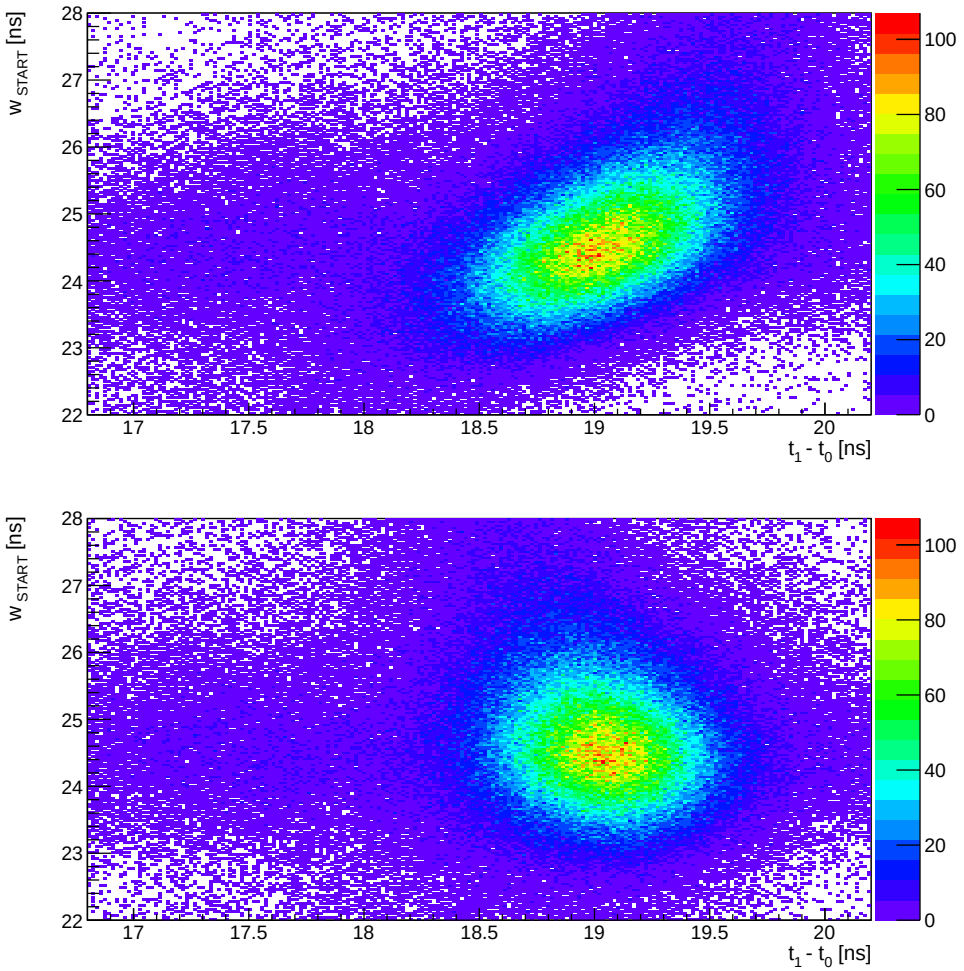

Figure 3.5: Dependence of time difference $t_1 - t_0$ on the width of the pulses measured by the START detector before time-walk correction (upper picture) and after the correction (lower picture).

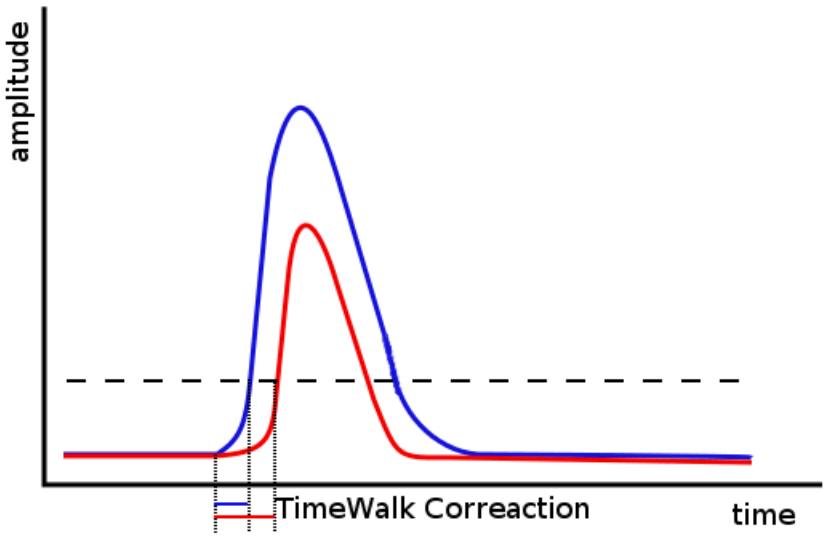

Figure 3.6: The time-walk correction scheme.

To summarise this method, one could see that the calibration was not so complicated - only selecting time difference $t_1 - t_0$ for each combination of START channel and Hodoscope rod and then shifting the mean value to presumed 19 ns. Thanks to the rather low interaction probability of the pions with target nuclei we had enough statistics in very short amount of time. That was the reason why during data taking we first performed this calibration method. The problem here might be not very good time resolution which tells us that the calibration parameters are determined with relatively big error bars.

3.2 Using electrons

This section will provide details of the second method that was implemented in order to obtain the pure START time resolution. This method is based on the measurement of the time of flight of electron-positron pairs (t_{e^-} resp. t_{e^+}) by one of the TOF or RPC detectors and the START detector (t_0 of the pion that interacted with the target). Identification of both leptons is done by the RICH detector. The reason why we use the electrons and positrones is that in the momentum acceptance of HADES spectrometer we can be sure that their speed is very close to the speed of light. From this fact and from well known distance of TOF and RPC detectors from target position we can easily deduce what should be the time of flight of these particles[2].

The process of calibration in this case was a little bit more difficult. First obstacle we had to deal with is the statistics. Because of the pion beam intensity, the cross section of

[2]This would be in case that no magnetic field lies between target and time of flight detectors. However in real situation this is not the case and it is necessary to recalculate the length of particle trajectory from target to the registered hit in TOF or RPC, based on the information from MDC tracking system.

interaction pion with target nuclei with production of the vector mesons, the decay rate of vector mesons into electron-positron pair ($< 10^{-4}$) and the detection efficiency of the pair ($\approx 90\%$), the needed data taking time was in order of tens hours. After the data taking it is necessary to produce ROOT files with the complete information about all particle candidates registered and identified by standard HADES analysis. The spectrum of particle candidates is shown in figure 3.7. Using cut on the region of electrones and positrones (this cut was rather wide so we do not lose a lot of statistics) plus the identification from RICH detector we separated very clean sample. Then for each particle we took the time of flight information and the information which START channel was hitted with the pion and we got 36 gauss-like distributions that were fitted for each time of flight detection system (TOF and RPC), see figures 3.8 and 3.9. The calibration parameter is then the difference of the mean of the distribution and the teoretical value of the time of flight. Because of different distance of TOF (210 cm) and RPC (235 cm) from the target position the mean values are different. The final calibration parameter for one START channel is weighted average with weights equal to σ of the time of flight distribution for each detection system. From the figures one can clearly see that the START detector and target were not perfectly aligned which caused some problems that will be discused in chapter 4.

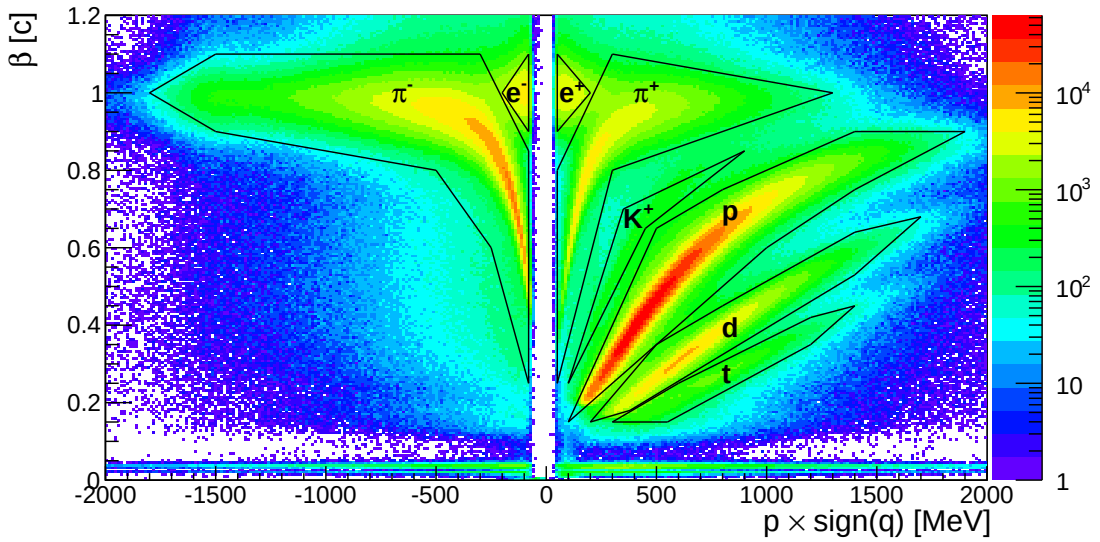

Figure 3.7: Plot with particle candidates showing the dependence of particle's velocity versus momentum times charge. Visible regions for different particle types are labelled. This plot contains $5.5 \cdot 10^7$ detected particles during one day with tungsten target.

The goal lies in finding the total time resolution $\sigma_{\mathrm{START+ToF}}$ from the distribution of $t_{\mathrm{e}^\pm}$ and also the time resolution of TOF/RPC detector[3] from the distribution of $t_{\mathrm{e}^+} - t_{\mathrm{e}^-}$.

[3]Because $t_{\mathrm{e}^\pm} = t_\pm - t_0$ (where $t_\pm$ is the measured time by the TOF/RPC detector of the positron/electron), $t_{\mathrm{e}^+} - t_{\mathrm{e}^-} = t_+ - t_-$ and it can be seen that this difference is not influenced by the measurement of the START detector.

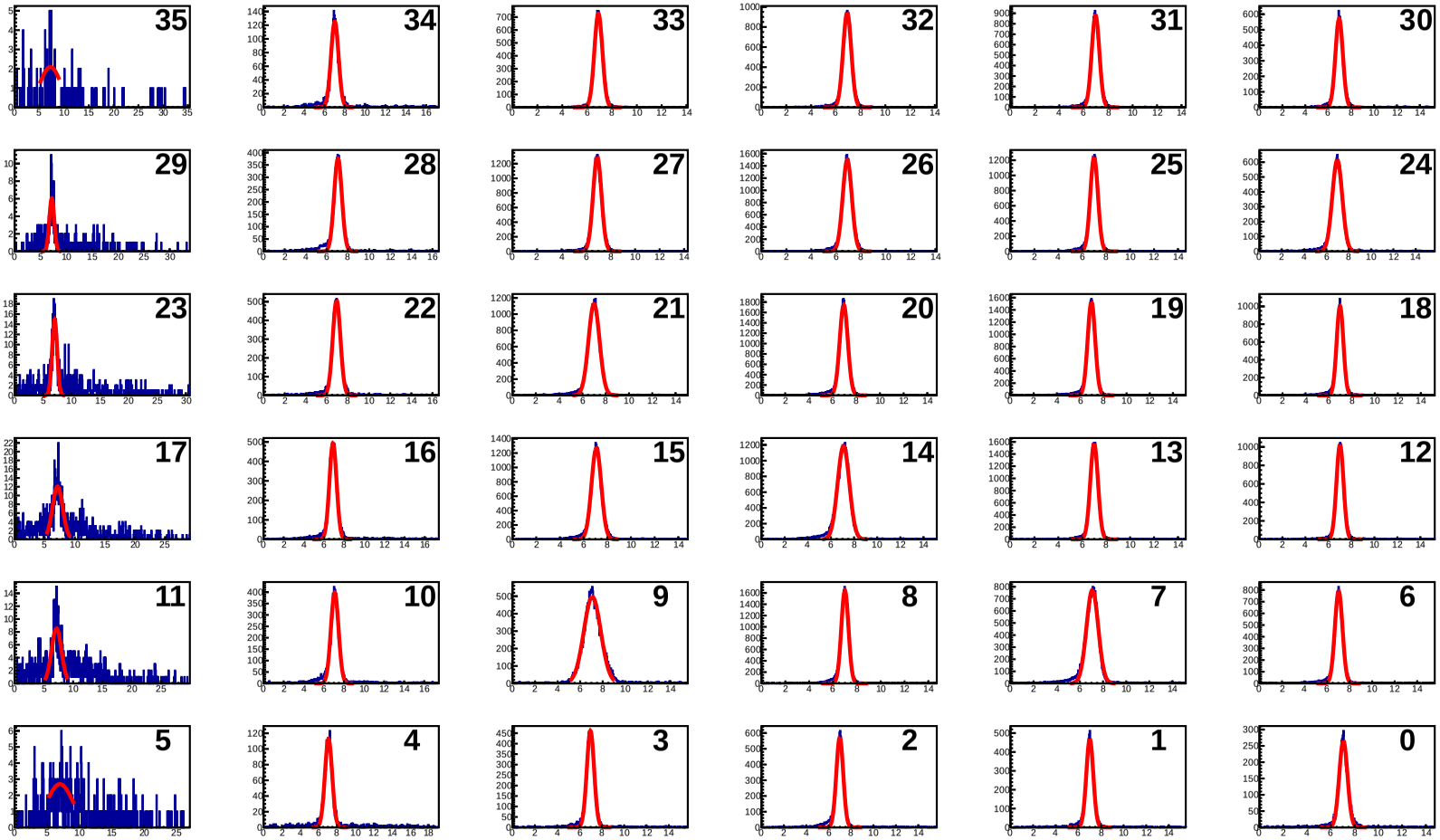

Figure 3.8: Fitted time of flight distributions between each START channel and TOF detector for electrones/positrones. On x-axis there are the times of flight in ns and on y-axis are number of particles. The number of START channel is shown in the top right corner of each plot.

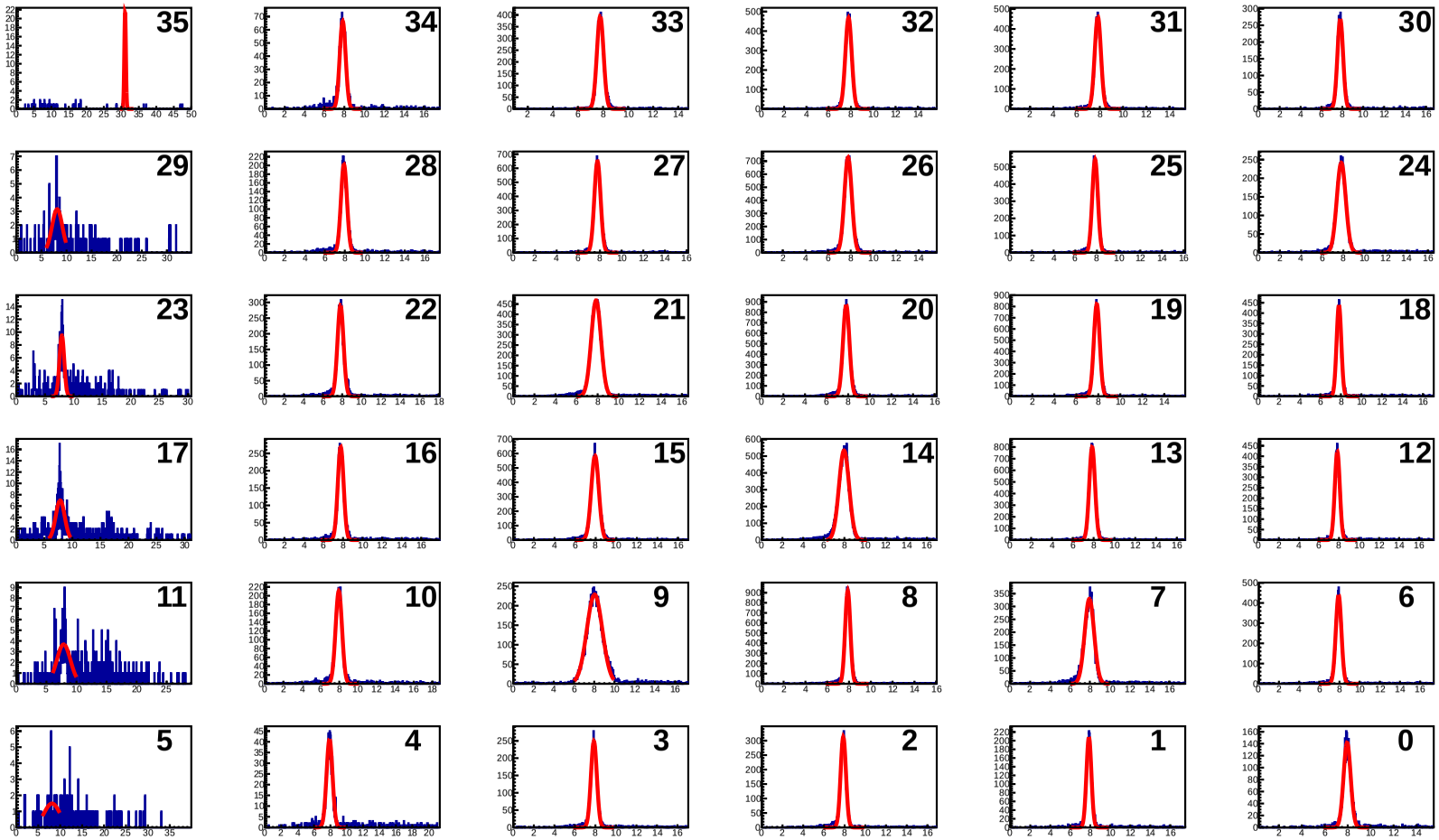

Figure 3.9: Fitted time of flight distributions between each START channel and RPC detector for electrones/positrones. On x-axis there are the times of flight in ns and on y-axis are number of particles. The number of START channel is shown in the top right corner of each plot.

It should be noted that from this distribution $\sigma = \sqrt{2} \cdot \sigma_{\mathrm{ToF}}$ is obtained since two particles are detected. It is then simple to get the pure time resolution of the START detector from

$$\sigma_{\mathrm{START}} = \sqrt{\sigma^2_{\mathrm{START+ToF}} - \sigma^2_{\mathrm{ToF}}}. \tag{3.2}$$

In all following pictures the symbol $\times$ for TOF data and $+$ for RPC data are used. The distribution of σ_{ToF} (time resolution) of the TOF/RPC detector depending on the START channel number through which the pion that interacted with the target flew and (gaving the electron/positron pair) is shown in figure 3.10. As can be seen the distribution is independent of the START channel number as it was expected (except few strips where there was a problem with statistics).

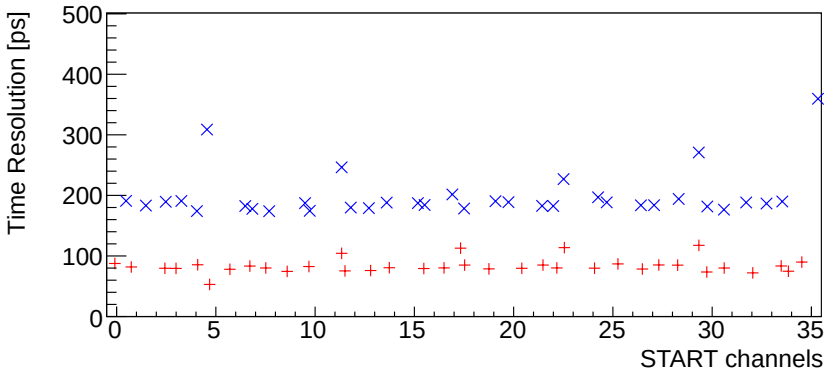

Figure 3.10: Time resolution of the TOF/RPC detector for each START channel.

Figure 3.11 shows the sequence of steps for the calculation of the time resolution for each START channel [4]. In the upper figure, the distributions of $\sigma_{\mathrm{START+ToF}}$ can be seen. From Fig. 3.10 it is known that the time resolution of the TOF detector is worse than of the RPC detector and this is the reason why blue points are seen above the red ones. The middle figure shows the pure START time resolution (σ_{START}) and the lower figure shows the same time resolution but after the application of time-walk corrections described in section 3.1. The average time resolution of the START detector is again $\sigma_{\mathrm{START}} \approx 170\,\mathrm{ps}$ which corresponds with the result of section 3.1 but unfortunatelly is worse that expected.

[4] Big differences in time resolutions are due to the different number of counts on each channel.

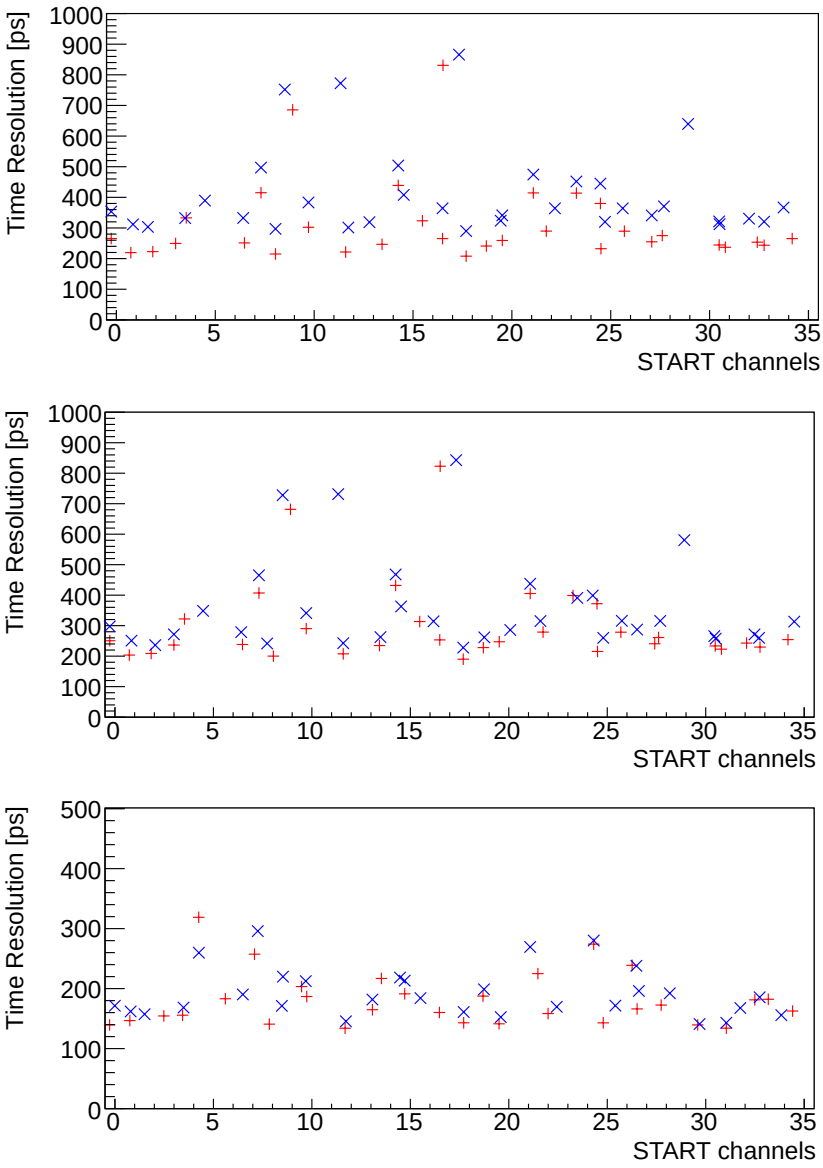

Figure 3.11: Time resolution of the START detector. On the upper picture it is shown the dependence of $\sigma_{\mathrm{START+ToF}}$ on START channel, on the middle one there is already pure START resolution σ_{START} but without the time-walk correction and on the lower picture is START time resolution after the correction.

CHAPTER 4

Elastic scattering $\pi^- + \mathrm{p} \rightarrow \pi^- + \mathrm{p}$

The elastic scattering of pion on proton is nowadays well know process thanks to a long history of research (already since late 1950's). Usual experimental setup is pion beam and the liquid hydrogen target. In the case of HADES pion beam experiment there were problems with the cooling system of the liquid hydrogen target and with background coming from the interactions with the target holders (seen in simulations). Therefore the decision was made that we will use instead polyethylene target ($[C_2H_4]_n$). The idea was that with the reference measurement with carbon target we can estimate the carbon contribution in polyethylene and after the subtraction we will get clear spectrum from interactions of pions with hydrogen. One can see how this works in section 4.1.

The analysis of known process is still interesting for present experiments as HADES because it can be used for normalisation. The process of normalisation can be explained as a kind of mapping between generally used physical variables (in this case it is cross section of reaction) and particular experimental result obtained with unique detector (number of events that were registered and their input and output particles corresponds with the reaction of interest). This topic will be discussed in more detail in section 4.2. There is also mentioned the agreement of simulations and measurements.

The final section of this chapter (section 4.3) contains the analysis of dynamics of the elastic scattering of pions on protons. Because during the second half of HADES pion beam experiment[1] the momentum of the pion beam has been changed several times it is interesting to look at the momentum of the scattered pions and compare their properties with calculations.

In the following I will use the standard units used in particle physics ($c = 1$ and $\hbar = 1$),

[1]The first half of the experiment was dedicated to the production and measurement of hadrons with strange quark (the pion beam momentum was set to the value above ϕ meson threshold production). During the second half the stress was put on the investigation of properties of the baryonic resonances ($N(1250)$ and $N(1535)$).

the metric tensor

$$g_{\mu\nu} = \begin{pmatrix} +1 & 0 & 0 & 0 \\ 0 & -1 & 0 & 0 \\ 0 & 0 & -1 & 0 \\ 0 & 0 & 0 & -1 \end{pmatrix}$$

and the notation used for four-momentum vector will be $P = (E, \vec{p})$ and for the magnitude of three-vector $p = |\vec{p}|$.

4.1 Subtraction of carbon contribution

When we need to distinguish between elastic scattering

$$\pi^- + \mathrm{p} \to \pi^- + \mathrm{p} \tag{4.1}$$

and quasi-elastic scattering

$$\pi^- + \mathrm{C} \to \pi^- + \mathrm{p} + \mathrm{X} \tag{4.2}$$

we can use the difference between azimuthal angle φ of the final state pion and proton. The difference $\Delta\varphi = |\varphi_\pi - \varphi_\mathrm{p}|$ would be in ideal case of elastic scattering (4.1) Dirac's δ-function at 180° thanks to the law of momentum conservation. From real experiment we expect that this distribution would be smeared to normal distribution due to finite spatial resolution and random fluctuations. The quasi-elastic scattering (4.2) on the other hand has a flatter distribution over the interval of possible values of $\Delta\varphi$ because of the presence of residual particles in the final state. Second option is to calculate the missing mass spectrum of π^-p pair

$$m^2_\mathrm{miss} = g_{\mu\nu}(P_\mathrm{out} - P_\mathrm{in})^\mu (P_\mathrm{out} - P_\mathrm{in})^\nu \tag{4.3}$$

where the Lorentz vector P_in of the incoming beam pion and one proton from target (neglecting the thermal motion of nucleons) can be described by

$$P_\mathrm{in} = \left(\sqrt{m_\pi^2 + p^2_\mathrm{beam}} + m_\mathrm{p}, \vec{p}_\mathrm{beam} \right) \tag{4.4}$$

and the out going Lorentz vector P_out of pion and proton is equal to

$$P_\mathrm{out} = \left(\sqrt{m_\pi^2 + p_\pi^2} + \sqrt{m_\mathrm{p}^2 + p_\mathrm{p}^2}, \vec{p}_\pi + \vec{p}_\mathrm{p} \right). \tag{4.5}$$

The expected value of m^2_miss for elastic scattering events is zero because in this case we detect all particles that participated in the reaction.

To subtract the number of elastic and quasi-elastic scattering events we have to compare the properties of two different targets. The graphical visualisation of used targets is on figure 4.1. The number of each event type can be calculated as

$$N_\mathrm{event} = N_\mathrm{beam} \cdot \sigma \cdot n_\mathrm{target} \cdot l_\mathrm{target} \tag{4.6}$$

where N_{beam} is the number of incoming beam particles, σ is the cross section of the studied reaction, l_{target} is the length of the target and n_{target} is density of scattering centres inside the target. This quantity is defined as

$$n_{\text{target}} = \frac{\rho \cdot N_A}{M} \tag{4.7}$$

where ρ is the mass density of target material, N_A is Avogadro constant and M is the molar mass of the target material. Knowing these variables for both of our targets, see table 4.1, we need to know the variable N_{beam} to be able to subtract the quasi-elastic events.

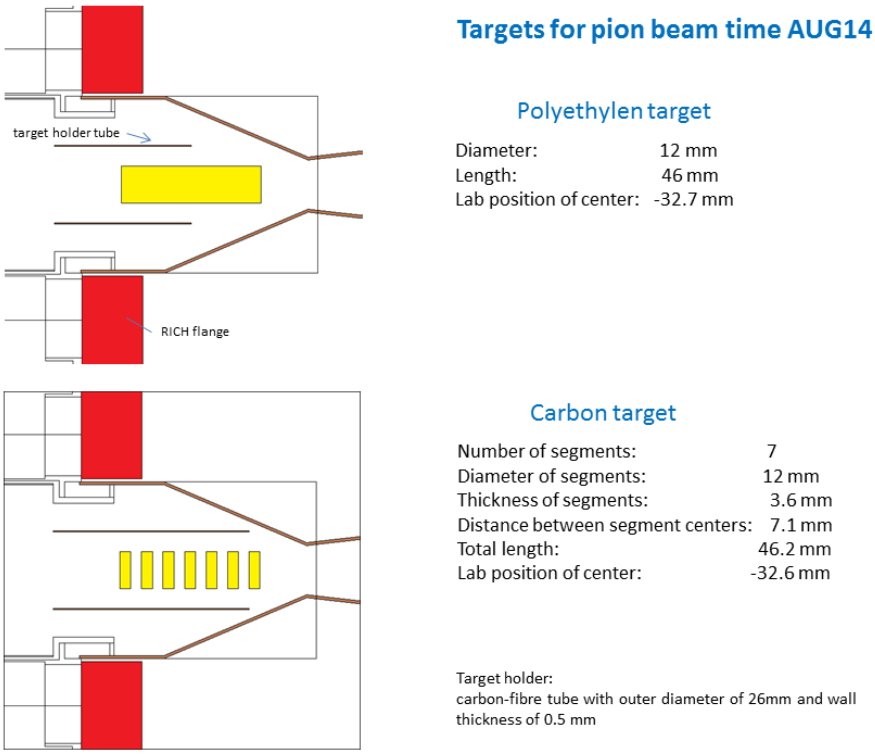

Figure 4.1: The scheme drawing of used targets - carbon and polyethylene, including the dimensions of targets. Prepared by Ilse Koenig.

target	polyethylene	carbon
chemical properties	$[C_2H_4]_n$	amorphous
molar mass [g/mol]	28.0	12.0
mass density [g/cm^3]	0.925	1.85
total length [cm]	4.6	2.52

Table 4.1: Properties of targets used in the second part of the HADES pion beam experiment.

The normalisation of the number of beam particles N_{beam} is not that easy. In front of the targets was placed the START detector but there was a small misalignment between

the detector and the target as one can see from figures 3.8 and 3.9. From these figures we concluded that beam pions going through one column of START channels does not interact with the target because there are almost none e^+/e^- pairs from these pions. However we know that the beam spot at START position was wide enough to cover whole START detector, this is shown on figure 4.2, and so there is a problem with measurement of the number of beam pions. All HADES channels are read out only when the trigger decision comes from the CTS, that would mean that we do not know exactly how many pions during the beam time passed through the target because we would measure only these that interacted when the detector was able to register outgoing particles from reaction (there is some dead time in which the reaction can happen but we would not know about it). Luckily the information if some particle is detected by START at anytime is stored in so called scalers and that means we know the total number of beam pions. But due to the mentioned misalignment we can not be sure how many of these pions could not interact with the target. That means we have to introduce some free parameter k which will multiply the measured number of detected pions to get the correct number of events of elastic scattering. This free parameter k can be different for each measured beam pion momentum because the focusing has been changed for each momentum.

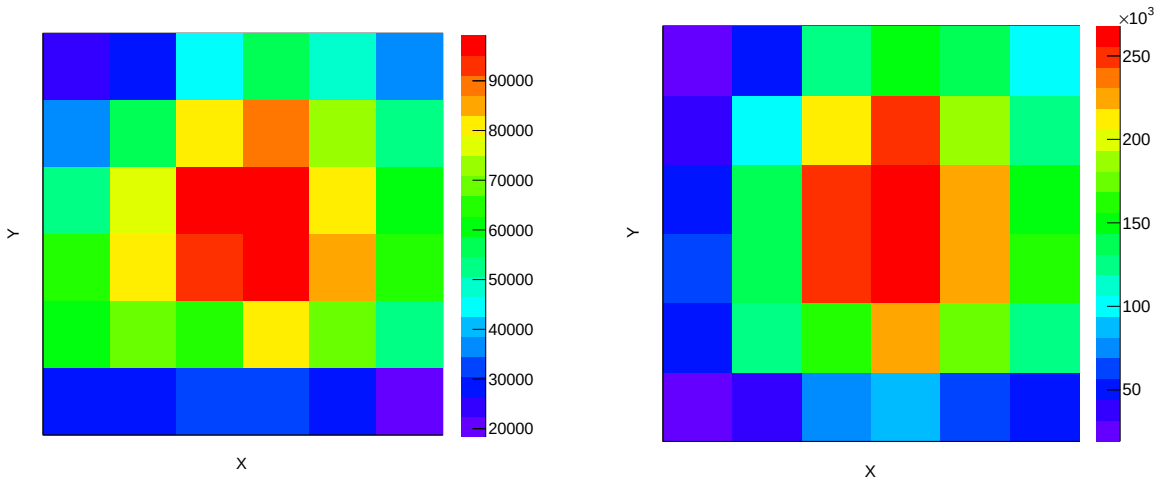

Figure 4.2: Beam spot at the START detector position. The left plot shows the beam spot for pions outside the reaction (no bias) and the right plot shows the beam spot for pions that interact with the target.

However what we really need are not these k-factors but to subtract $N^{\mathrm{C}}_{\mathrm{event}}$ number of interactions of pion with carbon from $N^{\mathrm{PE}}_{\mathrm{event}}$ number of interactions of pion with polyethylene to get pure number of elastic scattering events $N^{\mathrm{H}}_{\mathrm{event}}$

$$N^{\mathrm{H}}_{\mathrm{event}} = N^{\mathrm{PE}}_{\mathrm{event}} - f \cdot N^{\mathrm{C}}_{\mathrm{event}}. \tag{4.8}$$

The factor f is so called scaling factor. In our case it must contains quotient

$$f_1 = \frac{k^{\mathrm{PE}} \cdot N^{\mathrm{PE}}_{\mathrm{START}} \cdot \left(1 - t^{\mathrm{PE}}_{\mathrm{dead}}\right)}{k^{\mathrm{C}} \cdot N^{\mathrm{C}}_{\mathrm{START}} \cdot \left(1 - t^{\mathrm{C}}_{\mathrm{dead}}\right)} \tag{4.9}$$

where $k \cdot N_{\mathrm{START}}$ is the number of START counter multiplied by the unknown factor k to get the number of beam pion that interacted with target as discussed above. Plus we need to make a correction on the dead time of the detector which is the factor $1 - t_{\mathrm{dead}}$. This first part is related to the fact that each measurement lasted different time. The second part describes the different properties of targets

$$f_2 = \frac{l^{\mathrm{PE}}_{\mathrm{target}} \cdot \frac{2\rho^{\mathrm{PE}}}{M^{\mathrm{PE}}}}{l^{\mathrm{C}}_{\mathrm{target}} \cdot \frac{\rho^{\mathrm{C}}}{M^{\mathrm{C}}}} \tag{4.10}$$

where the number 2 in the numerator is because the molecule of polyethylene consists of two carbon atoms. Finally the factor $f = f_1 \cdot f_2$ but unfortunately we are able to predict only the value of the $f_2 = 0.7823$ because of the unknown factors k in f_1 part. Measured values of variables N_{START} and $1 - t_{\mathrm{dead}}$ are in the table 4.2 where we included also the number of actually triggered events N_{trigger}.

	polyethylene target				carbon target			
p_{beam} [MeV/c]	656	690	748	800	656	690	748	800
N_{trigger} $[\cdot 10^7]$	5.061	101.267	9.998	6.956	4.893	13.404	5.338	5.602
N_{START} $[\cdot 10^9]$	2.915	47.118	4.525	3.004	3.056	6.431	2.608	2.505
$1 - t_{\mathrm{dead}}$	0.841	0.767	0.768	0.756	0.860	0.834	0.783	0.751

Table 4.2: Values of the scaling variables for each target and beam momentum.

The method we use to find the factor f is following. We use the spectrum of $\Delta\varphi$ as it was mentioned at the beginning of this section. The visible peak from the elastic scattering (4.1) is between angles $(175°; 185°)$ that means that we can scale the spectrum of $\Delta\varphi$ measured with carbon target to the spectrum measured with polyethylene target for angles $\Delta\varphi \in (0°; 175°) \cup (185°; 360°)$. Then we can use this found factor for subtracting number of events, according to the equation (4.8) for $\Delta\varphi \in (175°; 185°)$ and get the number of elastic scattering events. We can also apply this procedure on the missing mass spectrum. In this case we use the part corresponding to $m^2_{\mathrm{miss}} \in (-0.6; -0.02)\,\mathrm{GeV^2/c^4}$ for calculating the scaling factor f because in the range $m^2_{\mathrm{miss}} \in (-0.02; 0.01)\,\mathrm{GeV^2/c^4}$ are the elastic scattering events. There is second peak in missing mass spectrum that is caused by π^0 meson in the final state of interaction, the appropriate interval is $m^2_{\mathrm{miss}} \in (0.01; 0.06)\,\mathrm{GeV^2/c^4}$ and above this value there is again dominated contribution from interactions of pions with carbon. The numerical results for the factors can be found in table 4.3. One can notice that the values of scaling factors $f_{m^2_{\mathrm{miss}}}$ are systematically lower that $f_{\Delta\varphi}$. This difference can be caused by the different efficiency of reconstructed beam momentum from Pion Tracker as only for such events can be calculated missing mass, while $\Delta\varphi$ method does not use

information about incoming pion beam momenta. Further investigation is ongoing. The spectra are shown on figures 4.3 and 4.4.

For the final decision if examined event is elastic scattering (4.1) or interaction with carbon (4.2) we use both cuts on $\Delta\varphi \in (175°; 185°)$ and $m^2_{\mathrm{miss}} \in (-0.02; 0.01)\,\mathrm{GeV}^2/\mathrm{c}^4$. First we applied cut on $\Delta\varphi$ and afterwards on m^2_{miss} which means that we had to applied above mentioned procedure of finding the scaling factor f also on missing mass spectrum after $\Delta\varphi$ cut, see figure 4.5. The final scaling factor $f_{m^2_{\mathrm{miss}}|\Delta\varphi}$ is the result of this scaling and particular values are given in table 4.3.

p_{beam} [MeV/c]	656	690	748	800
$f_{\Delta\varphi}$	0.807	5.068	1.507	1.064
$\left(k^{\mathrm{PE}}/k^{\mathrm{C}}\right)_{\Delta\varphi}$	1.107	0.962	1.132	1.126
$f_{m^2_{\mathrm{miss}}}$	0.757	4.394	1.350	0.953
$\left(k^{\mathrm{PE}}/k^{\mathrm{C}}\right)_{m^2_{\mathrm{miss}}}$	1.038	0.834	1.014	1.008
$f_{m^2_{\mathrm{miss}}\|\Delta\varphi}$	0.768	4.583	1.353	0.963
$\left(k^{\mathrm{PE}}/k^{\mathrm{C}}\right)_{m^2_{\mathrm{miss}}\|\Delta\varphi}$	1.054	0.870	1.016	1.019

Table 4.3: Numerical values of the factors f and the resulting ratio $k^{\mathrm{PE}}/k^{\mathrm{C}}$.

4.2 Comparison with simulations and published data

In this section we would like to briefly compare the results of our analysis of measured data with available published data and Monte Carlo simulations. Let's first focus on the simulations. We used Monte Carlo event generator for hadronic interaction called PLUTO developed by researches from HADES collaboration [16]. As an input for the simulations we used the angular distributions taken from summary article [17] because we wanted the simulations to be as close to reality as possible. From measured data we exported coordinates of approximately $9 \cdot 10^6$ vertices (again with the aim to have realistic simulations) and for each of the vertices we used PLUTO to generate the elastic scattering event. Afterwards we used the HGEANT (GEANT simulation with HADES geometry) software tool to simulate the respond of HADES spectrometer. The final step was to use the HYDRA (HADES sYstem for Data Reduction and Analysis) software tool that reconstructs the track candidates from the HGEANT output data.

By comparison of input number of events and the reconstructed number of events from the simulations we can determine the correction factors that we will use to adjust the number of elastic scattering events from real data analysis. These factors has the origin in the specific acceptance of HADES spectrometer as well as the detection and reconstruction efficiency. For data normalisation we decided to use the differential cross section $\mathrm{d}\sigma/\mathrm{d}\Theta_{\mathrm{CM}}$ as a function of pion polar angle in the centre of mass frame. The spectra of correction factors as a function of Θ_{CM} are shown on figure 4.6. From the SAID database [18] we obtained the reference values of the differential cross section. These values are calculated using

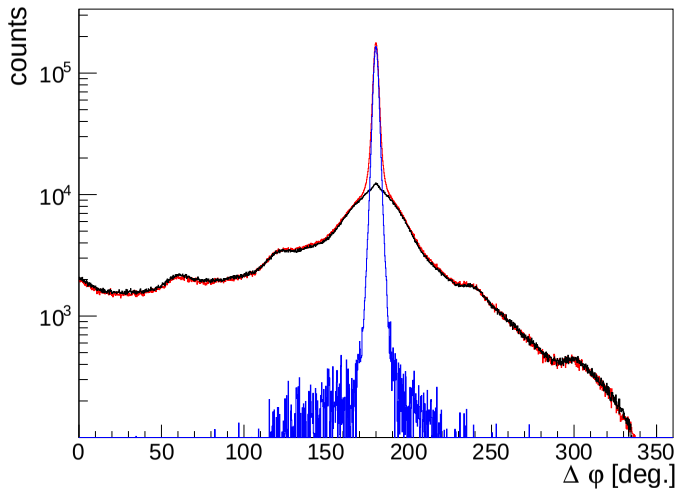

(a) $p_{\mathrm{beam}} = 656\,\mathrm{MeV/c}$

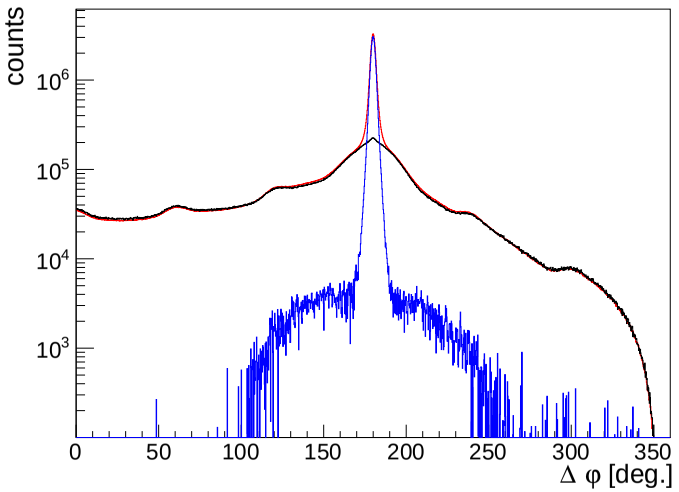

(b) $p_{\mathrm{beam}} = 690\,\mathrm{MeV/c}$

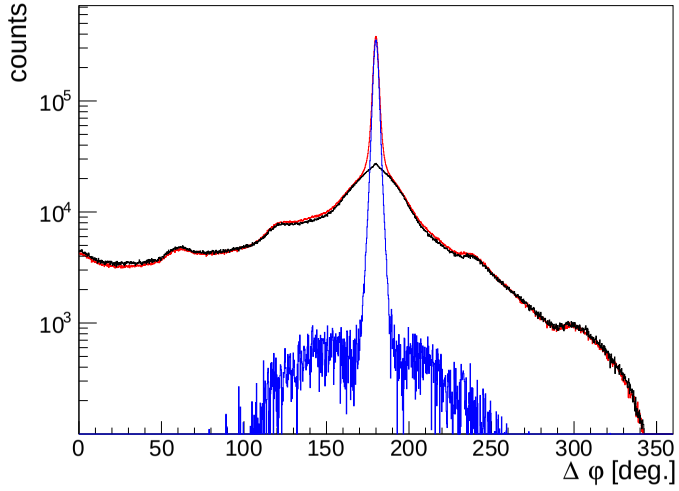

(c) $p_{\mathrm{beam}} = 748\,\mathrm{MeV/c}$

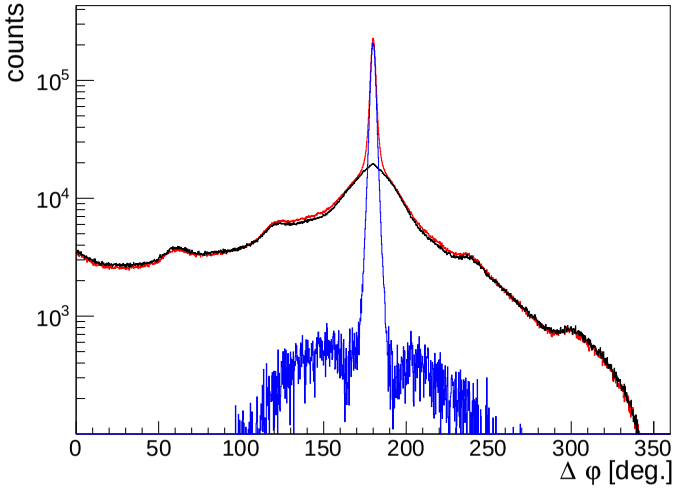

(d) $p_{\mathrm{beam}} = 800\,\mathrm{MeV/c}$

Figure 4.3: The pictures show measured $\Delta\varphi$ spectra with polyethylene target (red line) and scaled spectra for carbon target (black line). The subtracted spectrum $\mathrm{PE} - f_{\Delta\varphi} \cdot \mathrm{C}$ is displayed with blue line.

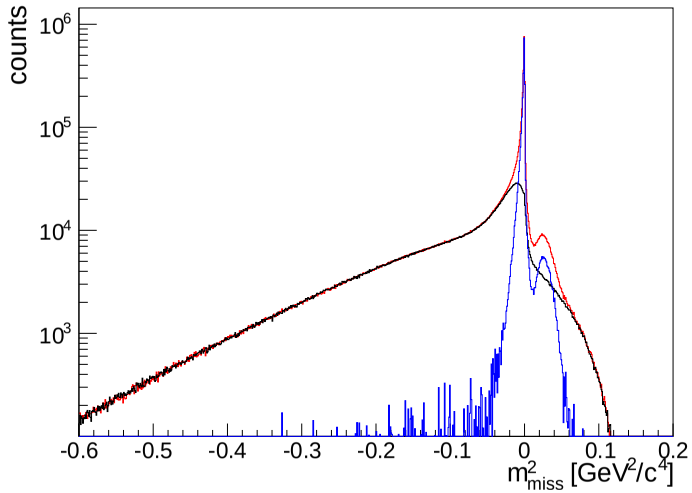

(a) $p_{\mathrm{beam}} = 656\,\mathrm{MeV/c}$

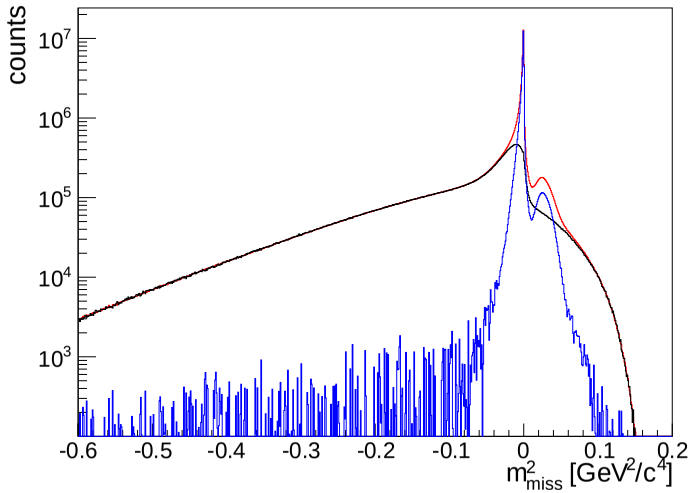

(b) $p_{\mathrm{beam}} = 690\,\mathrm{MeV/c}$

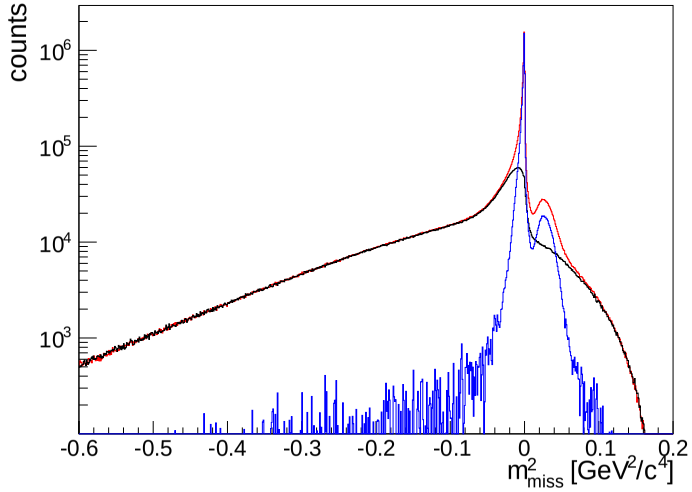

(c) $p_{\mathrm{beam}} = 748\,\mathrm{MeV/c}$

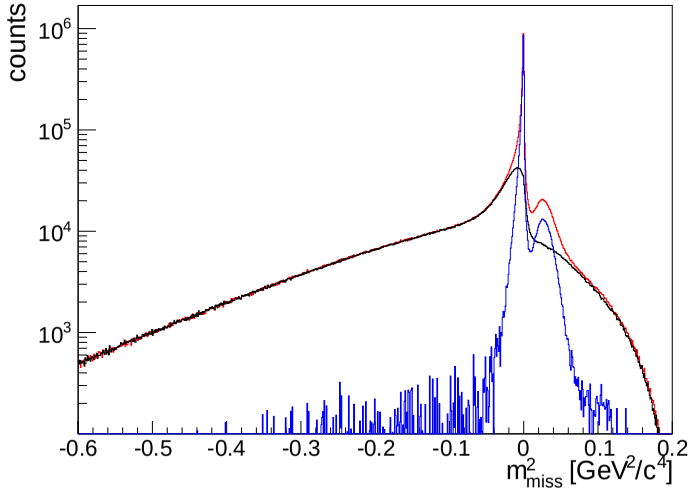

(d) $p_{\mathrm{beam}} = 800\,\mathrm{MeV/c}$

Figure 4.4: The pictures show measured m^2_{miss} spectra with polyethylene target (red line) and scaled spectra for carbon target (black line). The subtracted spectrum $\mathrm{PE} - f_{m^2_{\mathrm{miss}}} \cdot \mathrm{C}$ is displayed with blue line.

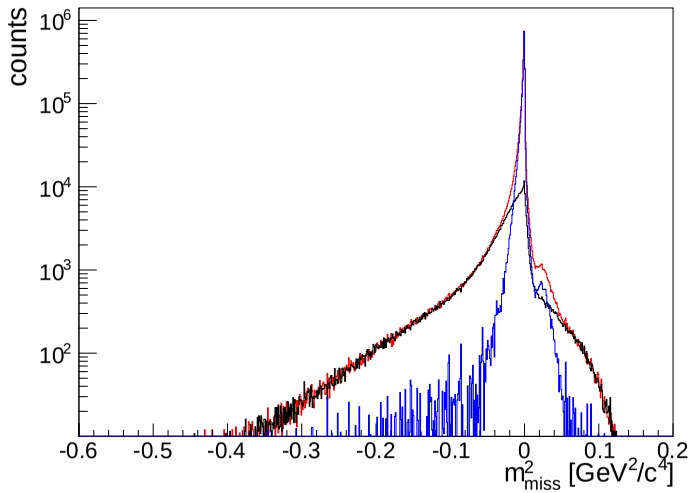

(a) $p_{\mathrm{beam}} = 656\,\mathrm{MeV/c}$

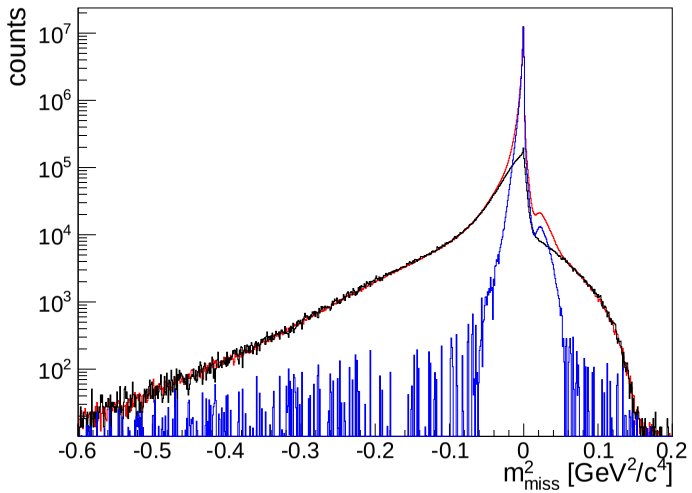

(b) $p_{\mathrm{beam}} = 690\,\mathrm{MeV/c}$

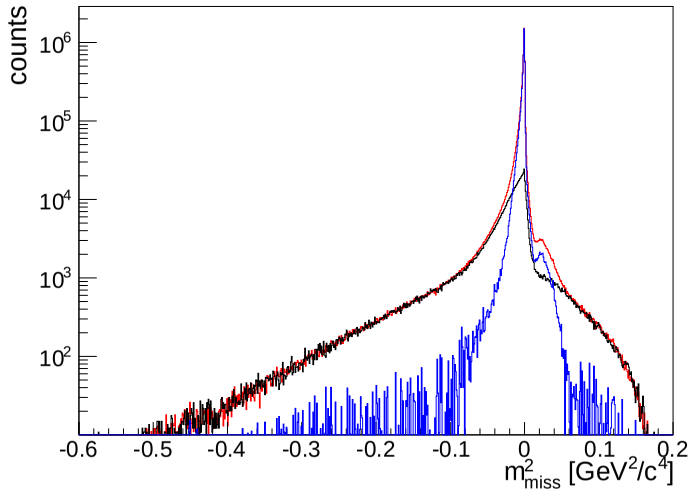

(c) $p_{\mathrm{beam}} = 748\,\mathrm{MeV/c}$

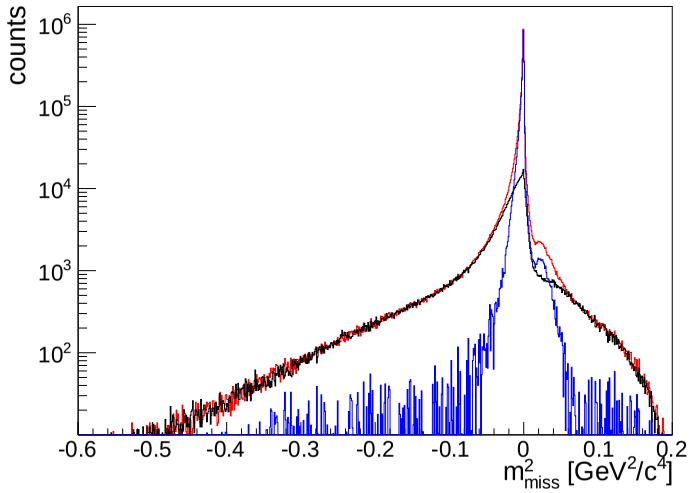

(d) $p_{\mathrm{beam}} = 800\,\mathrm{MeV/c}$

Figure 4.5: The pictures show measured m^2_{miss} spectra after cut $\Delta\varphi \in (175°; 185°)$ with polyethylene target (red line) and scaled spectra for carbon target (black line). The subtracted spectrum $\mathrm{PE} - f_{m^2_{\mathrm{miss}}} \cdot \mathrm{C}$ is displayed with blue line.

model WI08. The subtraction of carbon from polyethylene data is done using the $f_{m^2_{\mathrm{miss}}|\Delta\varphi}$ factor mentioned in section 4.1. We scaled our simulations and results from real data analysis in a way that they there will be the same cumulative differential cross section for $\Theta_{\mathrm{CM}} \in (50°; 100°)$ as for the data from SAID database. The final normalisation factors for differential cross section and the corrected number of elastic scattering events per number of registered beam pions can be found in table 4.4. One can see the result on figures 4.7 up to 4.10. From the figures it is visible that reconstructed number of elastic scattering events from real data analysis for $\Theta_{\mathrm{CM}} < 60°$ are below expectations from SAID database. A reason for this discrepancy might be that the published angular distribution [17] do not agree with the SAID database (there are differences between the lines in figures). As a consequence of this also the corrections factors might be different. Other effect that plays a role is a broad spectrum of beam momentum, see figure 4.16 below, because in simulations and also in the calculations of model used by SAID we presume perfectly narrow beam momentum distribution. The spread of p_{beam} cause that some interactions have very different collision energy. Due to the fact that we examine the region of baryonic resonances even small change in collision energy might have huge effect on the differential cross section. The measured values for $\Theta_{\mathrm{CM}} < 45°$ and $\Theta_{\mathrm{CM}} > 105°$ are influenced by boarder effects of the detectors that might not be perfectly described in simulations and can cause a lower detection efficiency.

p_{beam} [MeV/c]	656	690	748	800
c_{norm} [1/mb/rad]	4986.2	5200.0	4854.9	4689.7

Table 4.4: Numerical values of the normalisation factors.

We also compared our results for the total elastic scattering cross section σ_{el}. The reference (published) data were taken from [19] and we used 5^{th} order polynomial function for fitting these data in our region of interest $p_{\mathrm{beam}} \in (500; 900)\,\mathrm{MeV/c}$. One can see in figure 4.11 that the number of elastic scattering events normalised to the number of pions going through the START detector is not perfectly matching the fitted curve but the trend is the same. The agreement for beam momentum 748 MeV/c and 800 MeV/c is perfect but for 656 MeV/c and 690 MeV/c we observe less events. The difference between expected and measured value for $p_{\mathrm{beam}} = 656\,\mathrm{MeV/c}$ is approximately 18 % and for 690 MeV/c it is less than 8 %. The reason for these lower yields might be similar as in the case of differential cross section namely the problem of broad beam momentum distribution. Also as one can see from the upper plot in figure 4.11 the differences between reference points are sometimes very big which is due to complicated measurement of total cross section. In fact this is usually done in a way described in [17] that what is measured is differential cross section which is then fitted and the value of total elastic scattering is calculated from one of the fit parameter.

We tested the measurements if they agree with with simulation and the variable to be tested was particle momentum as a function of its polar angle in laboratory frame $p(\theta)$. The reason why we chose this dependence is because of a trivial φ distribution of particles

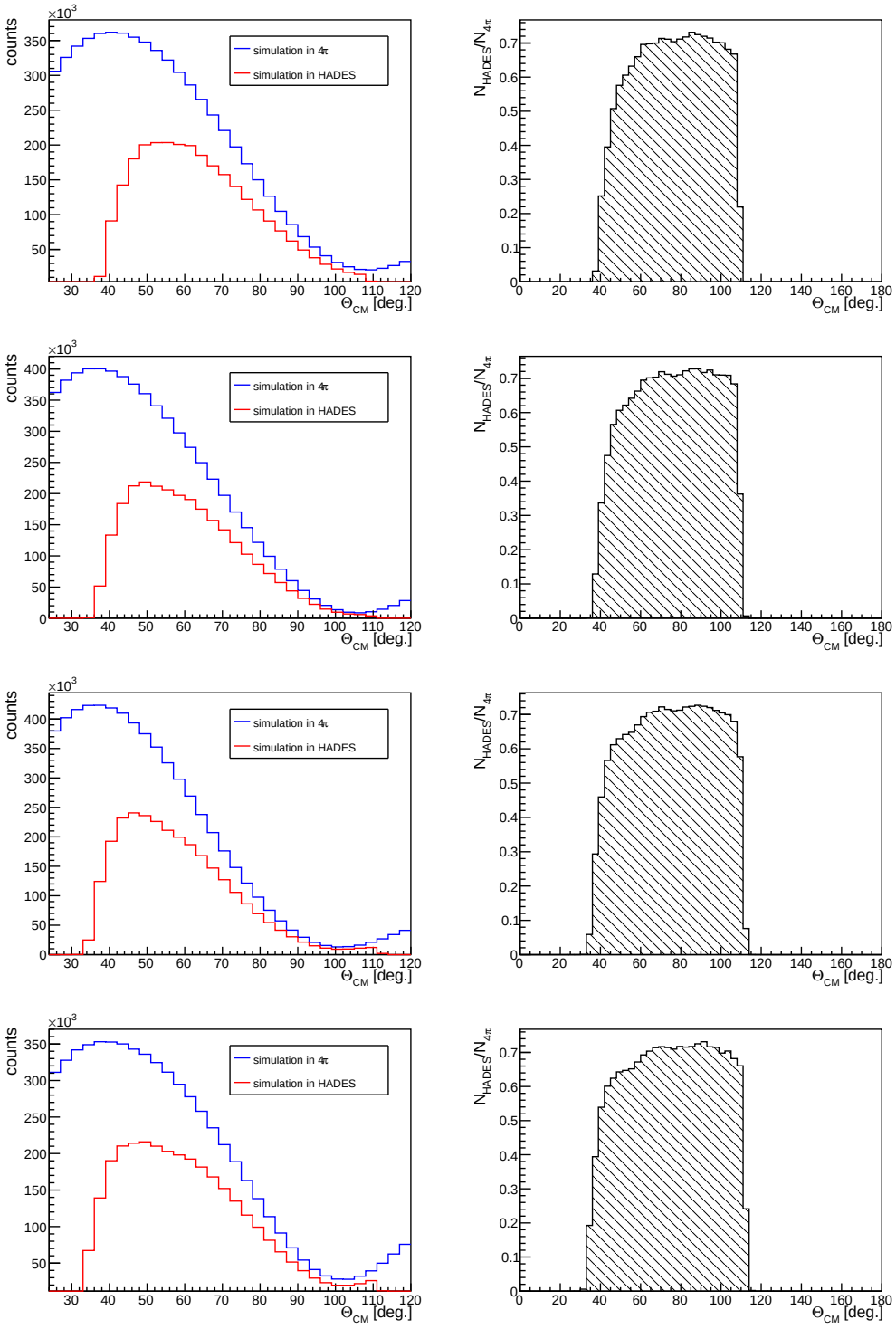

Figure 4.6: The spectra of correction factors are on the right side. On the left one can see the comparison between number of input events into simulations (blue line) and number of reconstructed events after whole simulation chain (red line). The plots are for measured beam momentum, from above 656, 690, 748 and $800\,\mathrm{MeV/c}$.

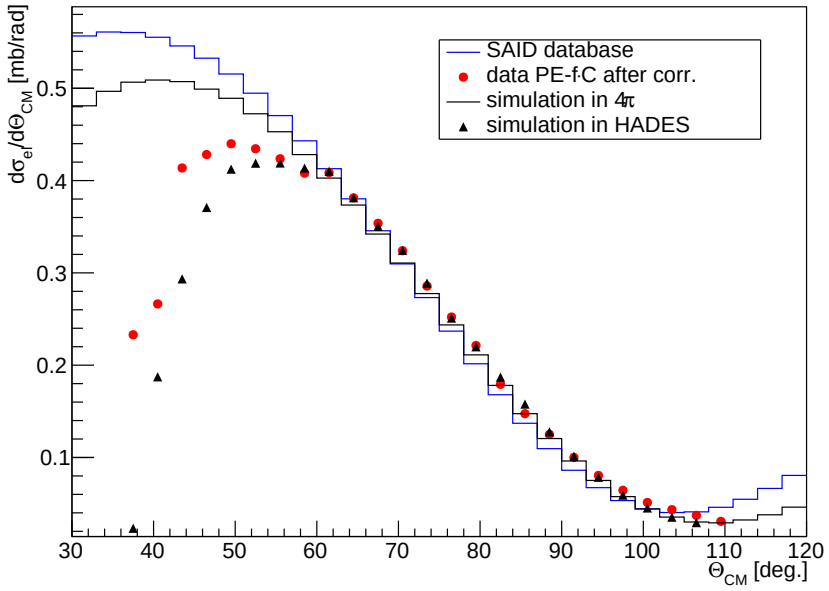

Figure 4.7: The spectra of differential cross section $^{\mathrm{d}\sigma}/_{\mathrm{d}\Theta_{\mathrm{CM}}}$ for $p_{\mathrm{beam}} = 656\,\mathrm{MeV/c}$.

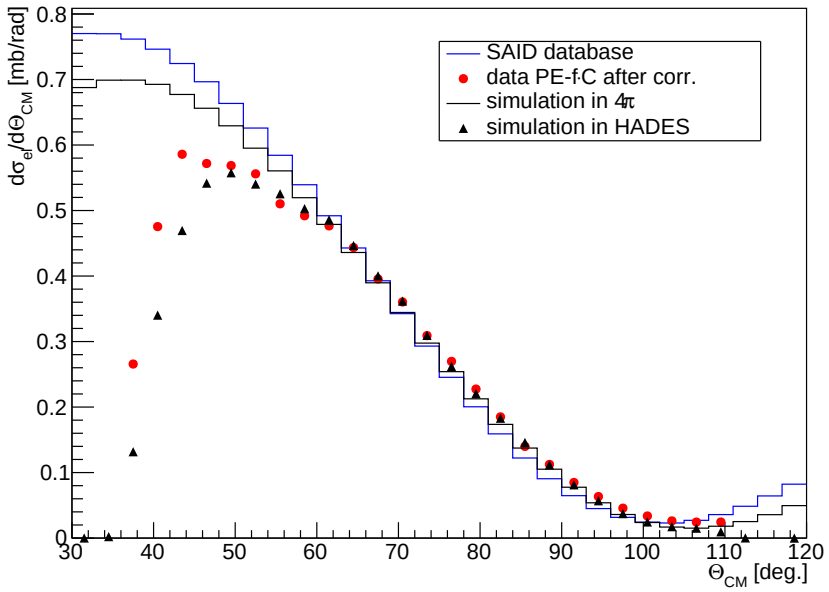

Figure 4.8: The spectra of differential cross section $^{\mathrm{d}\sigma}/_{\mathrm{d}\Theta_{\mathrm{CM}}}$ for $p_{\mathrm{beam}} = 690\,\mathrm{MeV/c}$.

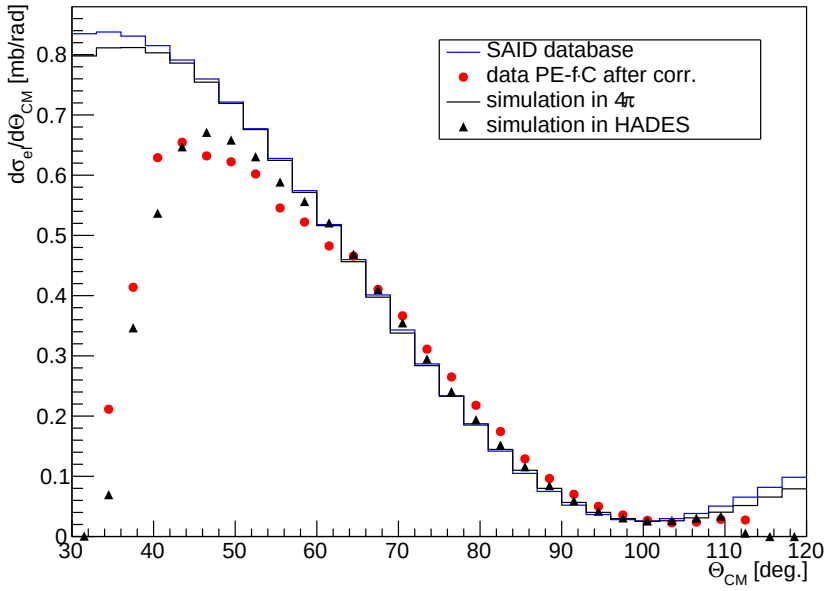

Figure 4.9: The spectra of differential cross section $^{\mathrm{d}\sigma}/_{\mathrm{d}\Theta_{\mathrm{CM}}}$ for $p_{\mathrm{beam}} = 748\,\mathrm{MeV/c}$.

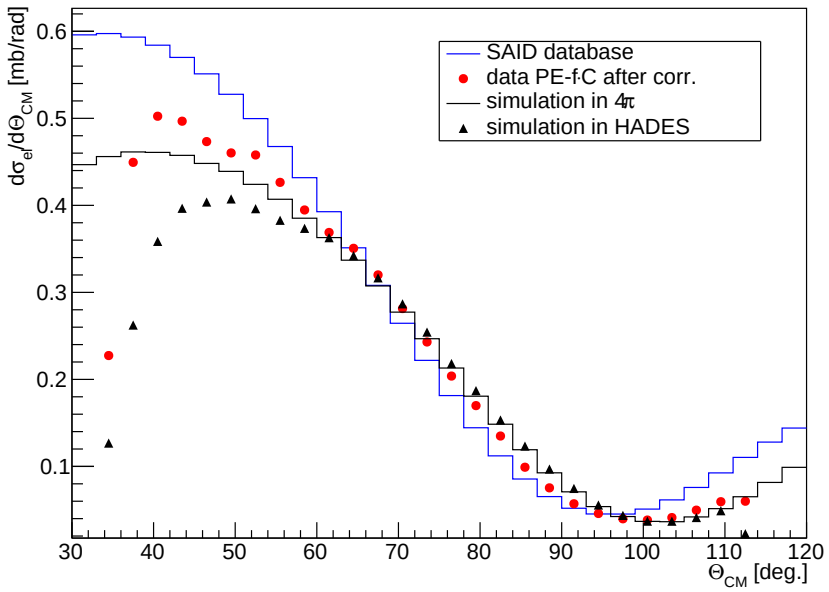

Figure 4.10: The spectra of differential cross section $^{\mathrm{d}\sigma}/_{\mathrm{d}\Theta_{\mathrm{CM}}}$ for $p_{\mathrm{beam}} = 800\,\mathrm{MeV/c}$.

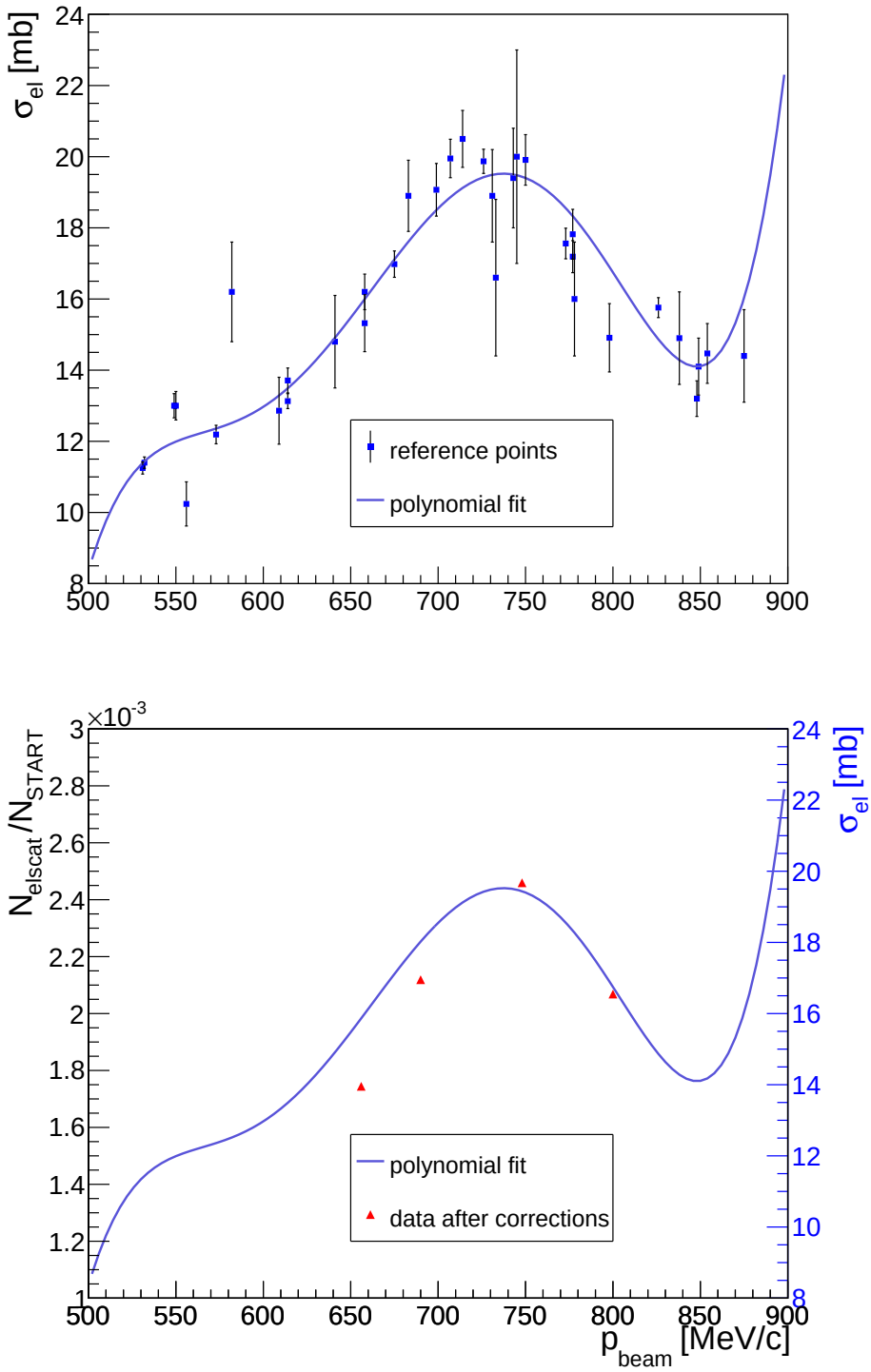

Figure 4.11: Comparison of published data and our measurement for cross section of elastic scattering $\pi^- + \mathrm{p} \rightarrow \pi^- + \mathrm{p}$.

from elastic scattering. The results are shown in figures 4.12 and 4.13. The figures in first columns show results from PLUTO generator so the dependence is just simple curve. In the second columns there are distributions obtained from complete simulations, i.e. PLUTO results goes through HGEANT and HYDRA. The acceptance and detection efficiency is therefore visible. Also the resolution in momentum measurement smeared the curve from first column into the shape of drop. The last columns are for analysis of real data. There is slightly more background events because in the simulations we have only elastic scattering events. We can not expect the 100 % selection efficiency of used cuts on $\Delta\varphi$ and m^2_{miss}. the drop shapes are also broader that the simulated ones because of the carbon contribution in the data (we are able to subtract the number of the elastic scattering events but not directly distinguish them). Still the agreement between simulations and real data is very good.

4.3 Momentum scan

Let's start with the kinematics of general elastic scattering. Simple drawing of the elastic scattering process is shown on figure 4.14. We will make our calculation in the rest frame of particle 2 because it naturally describes the situation with fix targets. Let us denote the particle masses m_1, m_2, the momentum before collision $\vec{p}_1$, $\vec{p}_2 = \vec{0}$ and after $\vec{p}_1'$, $\vec{p}_2'$. The angle between the vectors $\vec{p}_1$ and $\vec{p}_1'$ we shall mark as θ and the angle between $\vec{p}_1$ and $\vec{p}_2'$ as ω.

We can start only with the momentum conservation law

$$\vec{p}_1 = \vec{p}_1' + \vec{p}_2' \tag{4.11}$$

and the energy conservation law

$$E_1 + E_2 = E_1' + E_2' \tag{4.12}$$

where we have to use the relativistic relation between energy, momentum and mass $E = \sqrt{m^2 + p^2}$. Because of the rotational symmetry in angle φ of described problem we can solve the equation (4.11) as a set of two equations

$$\begin{aligned} p_1 &= p_1' \cos\theta + p_2' \cos\omega \\ 0 &= p_1' \sin\theta - p_2' \sin\omega. \end{aligned}$$

Now we will separate p_2' just on one side of the equations

$$\begin{aligned} p_1 - p_1' \cos\theta &= p_2' \cos\omega \\ p_1' \sin\theta &= p_2' \sin\omega \end{aligned}$$

and after squaring each equation and summing them together resulting

$$p_1^2 - 2p_1p_1' \cos\theta + p_1'^2 = p_2'^2 \tag{4.13}$$

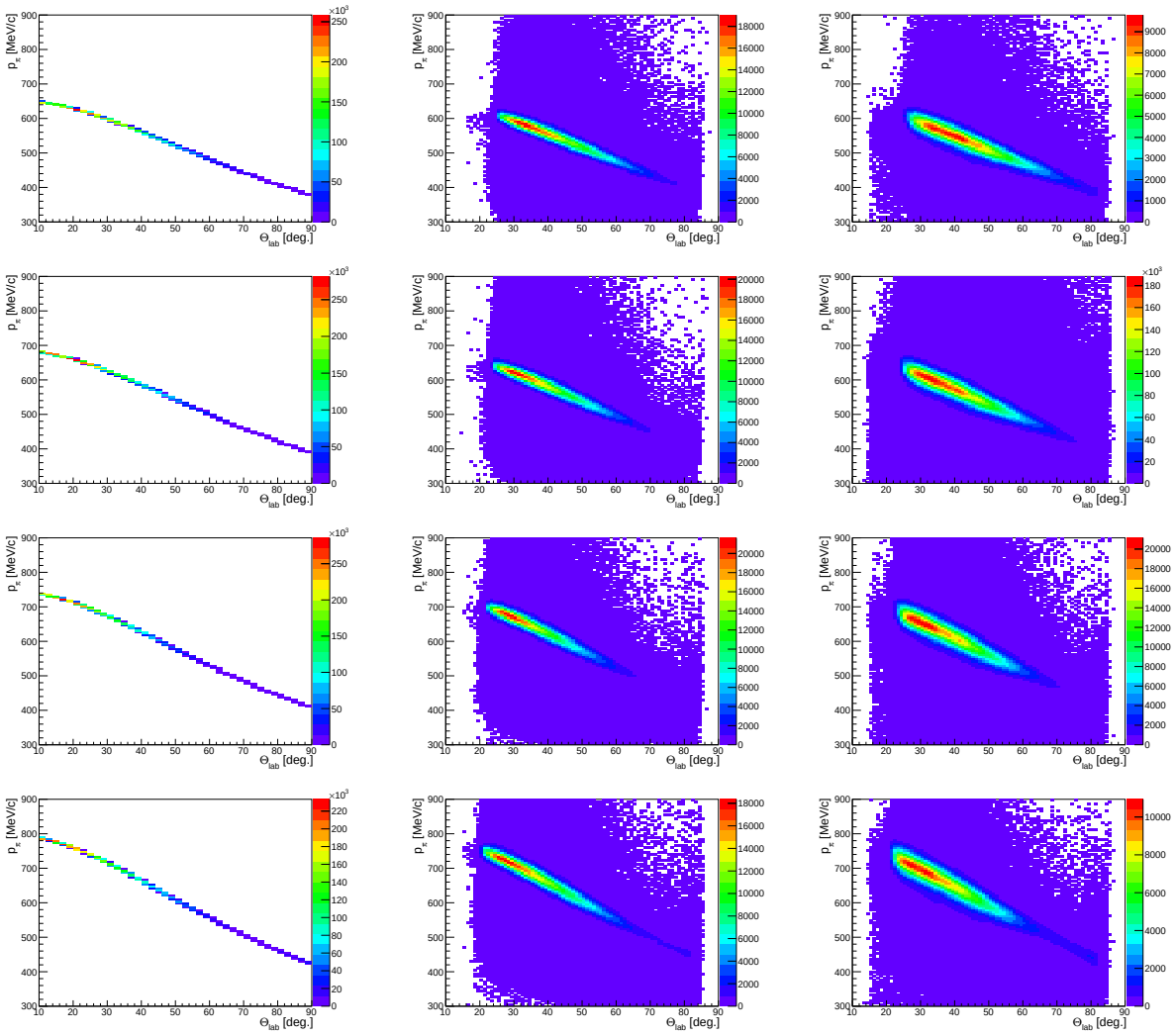

Figure 4.12: Scattered pion momentum distribution as a dependence on θ angle for different beam momentum, from above 656, 690, 748 and $800\,\mathrm{MeV/c}$. On left figures are results obtained from PLUTO generator, middle figures are for results of the simulations and right figures are showing results from measurement.

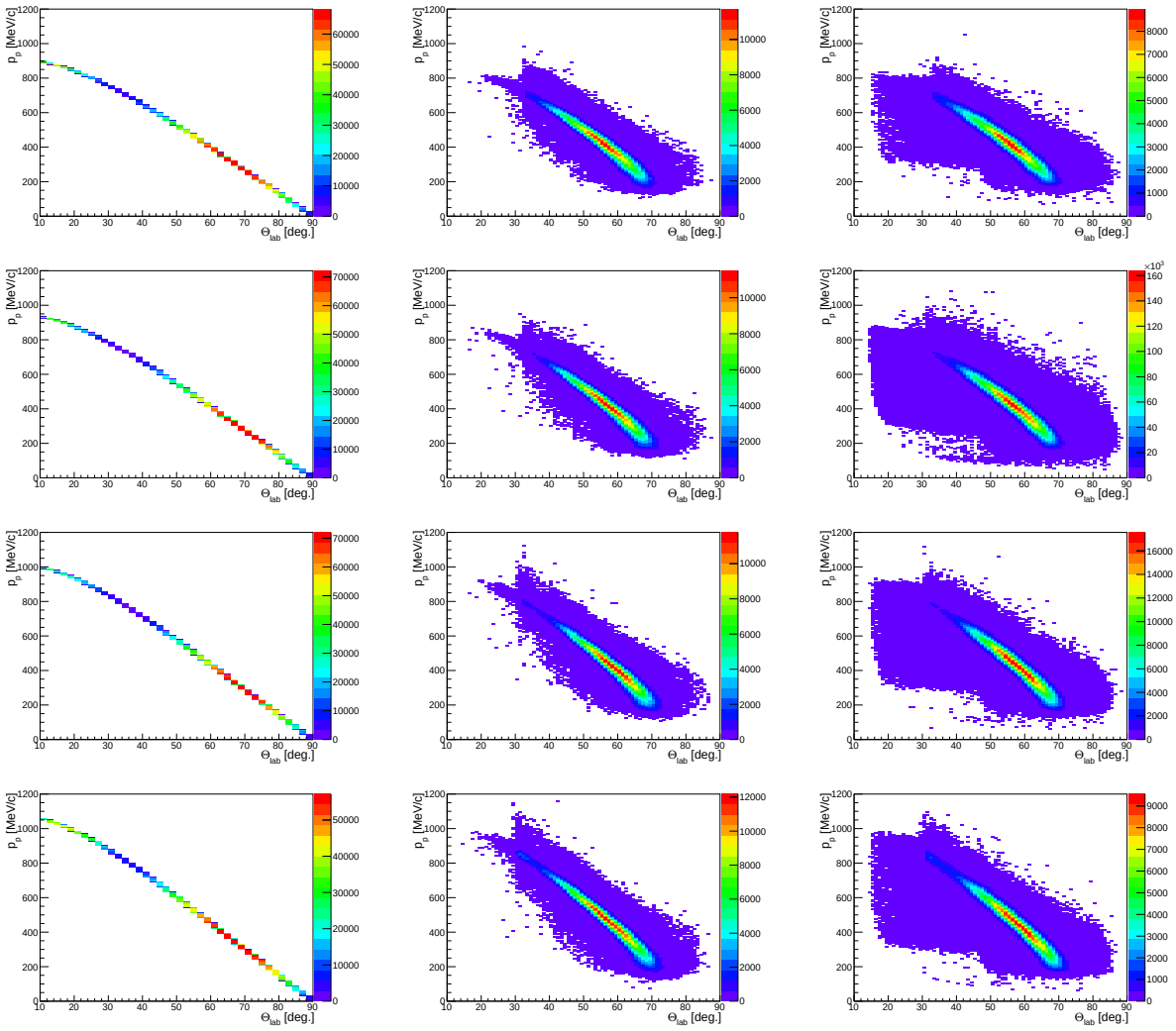

Figure 4.13: Scattered proton momentum distribution as a dependence on θ angle for different beam momentum, from above 656, 690, 748 and $800\,\mathrm{MeV/c}$. On left figures are results obtained from PLUTO generator, middle figures are for results of the simulations and right figures are showing results from measurement.

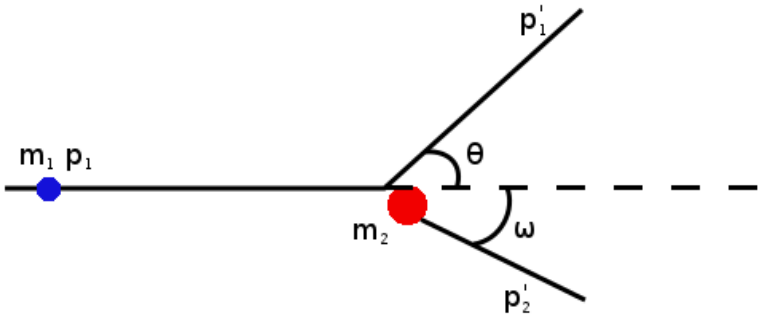

Figure 4.14: The scheme drawing of elastic scattering in the rest frame of particle 2.

thanks to the property of trigonometric functions $\sin^2\alpha + \cos^2\alpha = 1$. At this point we will take a look back on (4.12) which we will square and then we will get

$$p_1^2 + 2m_2\sqrt{m_1^2 + p_1^2} = p_1' + p_2' + 2\sqrt{m_1^2 + p_1'^2}\sqrt{m_2^2 + p_2'^2}. \tag{4.14}$$

Next we will substitute $p_2'^2$ in this equation by the left side of equation (4.13) and after one more squaring of the equation and a lot of algebraic a quadratic equation for p_1' occur

$$\begin{aligned} p_1'^2 \cdot \left[p_1^2\cos^2\theta - 2m_2\sqrt{m_1^2 + p_1^2} - m_1^2 - m_2^2 - p_1^2\right] + \\ + p_1' \cdot \left[2p_1\cos\theta m_2\sqrt{m_1^2 + p_1^2} + 2m_1^2 p_1\cos\theta\right] + \\ + 1 \cdot \left[m_2^2 p_1^2 - m_1^2 p_1^2\right] = 0. \end{aligned} \tag{4.15}$$

For shorter writing we will introduce the Mandelstam variable $s = m_1^2 + m_2^2 + 2m_2E_1$ so we can write

$$p_1'^2 \underbrace{\left(-p_1^2\sin^2\theta - s\right)}_{a} + p_1' \underbrace{\left[2p_1\cos\theta\left(m_2E_1 + m_1^2\right)\right]}_{b} + \underbrace{p_1^2\left(m_2^2 - m_1^2\right)}_{c} = 0. \tag{4.16}$$

When we treat the discriminant of this quadratic equation we find out that

$$D = b^2 - 4ac = \ldots = 4p_1^2\left(m_2 + E_1\right)^2\left(m_2^2 - m_1^2\sin^2\theta\right) \tag{4.17}$$

and the two solutions for p_1' are

$$(p_1')_{1,2} = \frac{-b \pm \sqrt{D}}{2a} = \ldots = p_1\frac{\left(s + m_1^2 - m_2^2\right)\cos\theta \pm 2\left(m_2 + E_1\right)\sqrt{m_2^2 - m_1^2\sin^2\theta}}{2\left(p_1^2\sin^2\theta + s\right)} \tag{4.18}$$

but we can take only the $^{-b+\sqrt{D}}/_{2a}$ solution because this gives positive value.

Now we can apply the equation (4.18) on the examined problem (4.1) where we will use $m_1 = m_\pi$, $\vec{p}_1 = \vec{p}_{\text{beam}}$, $\vec{p}_1' = \vec{p}_\pi$, $m_2 = m_{\text{p}}$ and $\vec{p}_2' = \vec{p}_{\text{p}}$. The measured interval of angle θ we

cut into smaller intervals each of them with 5° width. On these intervals we approximate the theoretical momentum distribution dependent on angle $p(\theta)$ with the value in the middle of the interval. And finally the calculated values are compared with the measured ones[2], this is shown in tables 4.5 up to 4.8 for values of θ angle in HADES acceptance.

The data in the tables show rather good agreement of our measurement but one can see that the average value of the differences $p^{\text{diff}} = p_\pi^{\text{calculated}} - p_\pi^{\text{measured}} = 11\,\text{MeV/c}$. We can explain part of this value if we take into account the energy losses of pion inside the polyethylene target. Even thought pions with momentum in examined range are in minimum ionising region we should count with the radiation losses. Using the PSTAR program [20] that calculates the stopping power for protons in materials we estimated the energy losses E_{loss}. For that we presumed that pions will interact likely as protons if both particles are MIPs. Then we calculated the kinetic energy of protons as they would have the same velocity β as the beam pions and then from the table in PSTAR program we found that for polyethylene the losses are $E_{\text{loss}} = 1.96\,\text{MeV/cm}$. The mean length of path that pions goes through the target we estimate as $1/2$ of the target length (4.6 cm) so the pion momentum losses inside the target are approximately 4.6 MeV/c. One can check this calculation on figure 4.15 where the distribution of pion momentum is depending on the z-coordinate of the interaction point.

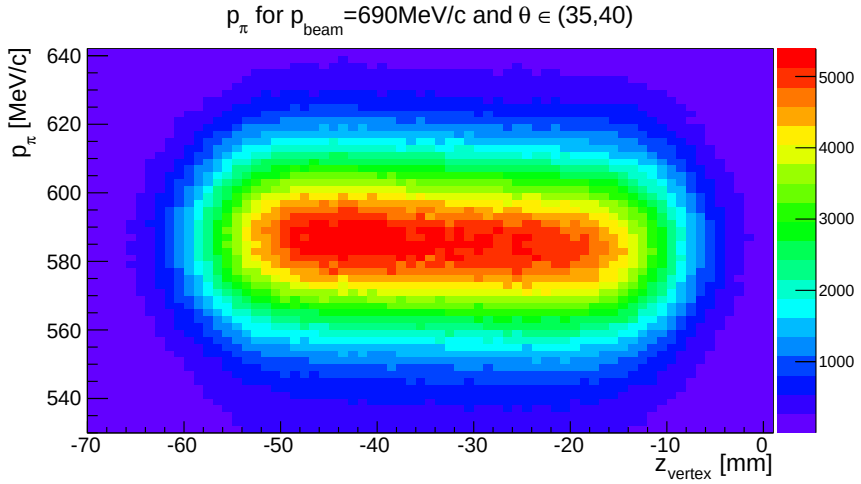

Figure 4.15: The spectra of reconstructed pion momentum depending on the z-coordinate of the vertex.

The remaining 6.4 MeV/c of the difference between measurement and expectation is not completely understand. The most probable explanation is based on the knowledge of used magnet optics along the beam line. The focusation was done in such a way that beam pions with higher momentum were registered in the top part of START detector and the low momentum pions were registered in the bottom part, see figure 4.16. And the reason

[2]Due to small error in known HADES magnetic field map, the reconstructed pion momentum is multiplied by factor 1.006 to obtain the correct one. This factor was found by colleagues from analysis of previous experiments but this analysis can give us an independent checkup.

$p_{\mathrm{beam}} = 656\,\mathrm{MeV/c}$			
centre θ [°]	$p_\pi^{\mathrm{calculated}}$ [MeV/c]	$p_\pi^{\mathrm{measured}}$ [MeV/c]	difference [MeV/c]
22.5	626.8	562.3	64.5
27.5	611.3	600.2	11.1
32.5	593.9	583.8	10.1
37.5	575.1	565.2	9.9
42.5	555.4	546.0	9.4
47.5	535.1	525.1	10.0
52.5	514.6	504.8	9.9
57.5	494.4	485.9	8.4
62.5	474.6	467.9	6.7
67.5	455.4	447.9	7.4
72.5	437.0	428.3	8.7
77.5	419.5	406.0	13.5
82.5	402.9	389.1	13.8

Table 4.5: Comparison of pion momentum measurement with theoretical prediction in elastic scattering events.

$p_{\mathrm{beam}} = 690\,\mathrm{MeV/c}$			
centre θ [°]	$p_\pi^{\mathrm{calculated}}$ [MeV/c]	$p_\pi^{\mathrm{measured}}$ [MeV/c]	difference [MeV/c]
22.5	664.9	636.8	28.1
27.5	647.6	629.0	18.6
32.5	628.2	610.5	17.7
37.5	607.2	590.3	16.9
42.5	585.3	569.8	15.5
47.5	562.9	546.7	16.2
52.5	540.4	525.0	15.4
57.5	518.2	504.9	13.3
62.5	496.5	484.5	12.0
67.5	475.6	463.6	12.0
72.5	455.6	441.5	14.1
77.5	436.7	417.6	19.1
82.5	418.9	401.0	17.9

Table 4.6: Comparison of pion momentum measurement with theoretical prediction in elastic scattering events.

$p_{\mathrm{beam}} = 748\,\mathrm{MeV/c}$			
centre θ [°]	$p_\pi^{\mathrm{calculated}}$ [MeV/c]	$p_\pi^{\mathrm{measured}}$ [MeV/c]	difference [MeV/c]
22.5	702.8	689.4	13.5
27.5	683.5	673.0	10.5
32.5	662.0	651.5	10.5
37.5	638.8	629.3	9.5
42.5	614.7	606.3	8.4
47.5	590.1	581.0	9.1
52.5	565.4	556.2	9.3
57.5	541.2	534.7	6.5
62.5	517.7	512.2	5.5
67.5	495.1	489.6	5.5
72.5	473.5	467.9	5.6
77.5	453.2	443.4	9.8
82.5	434.1	425.5	8.6

Table 4.7: Comparison of pion momentum measurement with theoretical prediction in elastic scattering events.

$p_{\mathrm{beam}} = 800\,\mathrm{MeV/c}$			
centre θ [°]	$p_\pi^{\mathrm{calculated}}$ [MeV/c]	$p_\pi^{\mathrm{measured}}$ [MeV/c]	difference [MeV/c]
22.5	751.5	735.1	16.4
27.5	729.5	715.5	14.0
32.5	705.1	691.4	13.7
37.5	679.0	666.8	12.2
42.5	651.8	640.9	10.9
47.5	624.3	612.9	11.4
52.5	596.9	586.3	10.5
57.5	570.0	562.3	7.7
62.5	544.1	538.0	6.1
67.5	519.2	514.3	4.9
72.5	495.7	488.5	7.2
77.5	473.5	462.5	11.0
82.5	452.8	442.1	10.7

Table 4.8: Comparison of pion momentum measurement with theoretical prediction in elastic scattering events.

why we reconstruct smaller values more often is that the beam spot on START detector was slightly shifted above the centre of START detector, i.e. we are loosing more pions with higher momenta as one can see on the right plot of figure 4.2.

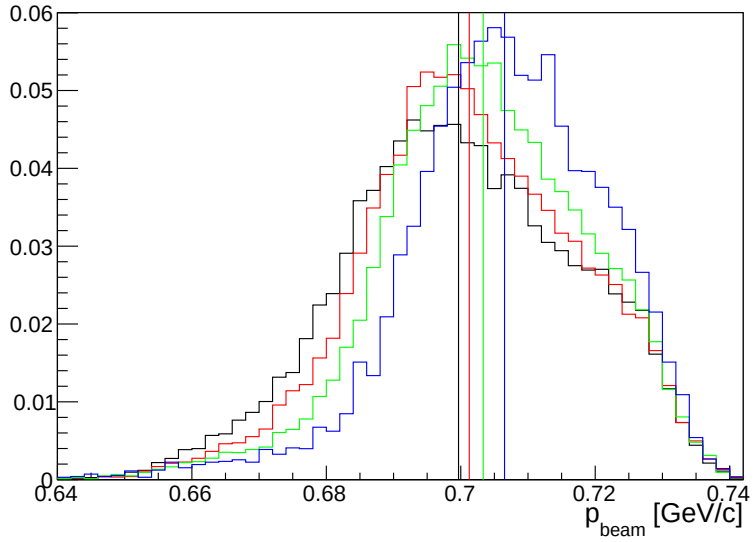

Figure 4.16: The normalised beam momentum distribution for different START channels. The black colour line is for the START channel #8, red line #14, green line #20 and blue line #26.

Conclusion

In this thesis is given the description of HADES pion beam experiment. In more detail the functionality and data analysis from beam line detectors is presented. The analysis of measured data with pion beam and polyethylene resp. carbon target is represented by the analysis of elastic scattering $\pi^- + \mathrm{p} \rightarrow \pi^- + \mathrm{p}$.

The first chapter contains general introduction into measurements with HADES spectrometer as well as in formations about the important subdetectors. The next chapter is dedicated to the Hodoscope as one of the beam line detectors. The testing and preparation of the Hodoscope for the pion beam experiment forms a main part of this chapter. The description of two methods of time calibration of the START detector is in the third chapter. Last chapter contains the data analysis of elastic scattering $\pi^- + \mathrm{p} \rightarrow \pi^- + \mathrm{p}$ together with the comparison with simulations and published data.

A valuable result of this work might be the normalisation of differential cross section which is the key point of section 4.2. As it was said this is important for research of unknown or rarely measured processes where they can use these normalisation constants and find the cross sections of examined processes.

Bibliography

[1] A. Kugler [HADES Collaboration], High acceptance di-electron spectrometer: Tool for study of hadron properties in the nuclear medium, *Czech. J. Phys.* **50/S2** (2000) 72-85.

[2] G. Agakishiev *et al.* [HADES Collaboration], The High-Acceptance Dielectron Spectrometer HADES, *Eur. Phys. J.* A **41** (2009) 243-277.

[3] HADES wikipedia, retrieved from `https://hades-wiki.gsi.de/` [online 2014, June 15].

[4] J. Pietraszko *et al.* [HADES Collaboration], Diamonds as timing detectors for minimum-ionizing particles: The HADES proton-beam monitor and START signal detectors for time of flight measurements, *Nucl. Instrum. Meth.* A **618** (2010) 121-123.

[5] J. Pietraszko *et al.* [HADES Collaboration], Radiation damage in single crystal CVD diamond material investigated with a high current relativistic ^{197}Au beam, *Nucl. Instrum. Meth.* A **763** (2014) 1-5.

[6] L. Fabbietti, *Study of the* e^+e^- *pair acceptance in the dilepton spectrometer HADES*: Doctoral thesis. Munich: Technische Universität München, Physics Department, 2003.

[7] J. S. Siebenson, *Exclusive analysis of the* $\Lambda(1405)$ *resonance in the charged* $\Sigma\pi$ *decay channels in proton proton reactions with HADES*: Master thesis. Munich: Technische Universität München, Physics Department, 2010.

[8] H. Alvarez Pol, *On the Multiwire Drift Chambers alignment of the HADES dilepton spectrometer*: Doctoral thesis. Santiago de Compostela: University of Santiago de Compostela, Faculty of Physics, 2002.

[9] T. Marek, *Detekce leptonů v reakcích relativistických těžkých iontů*: Master thesis. Prague: Charles University in Prague, Faculty of Mathematics and Physics, 1998.

[10] P. Cabanelas Eiras, *Software development and Performance Analysis of the HADES Resistive Plate Chamber Time-of-Flight Detector at GSI*: Doctoral thesis. Santiago de Compostela: University of Santiago de Compostela, Faculty of Physics, 2011.

[11] O. Svoboda *et al.* [HADES Collaboration], Electromagnetic calorimeter for the HADES@FAIR experiment, *JINST* **9** (2014) C05002.

[12] O. V. Andreeva *et al.* [HADES Collaboration], Forward scintillation hodoscope for nuclear fragment detection at the high acceptance dielectron spectrometer (HADES) setup, *Instrum. Exp. Tech.* **57** (2014) 103-119.

[13] J. Michel *et al.* [HADES Collaboration], The HADES DAQ system: Trigger and read-out board network, *IEEE Trans. Nucl. Sci.* **58** (2011) 1745-1750.

[14] J. Diaz *et al.*, Design and commissioning of the GSI pion beam, *Nucl. Instrum. Meth.* A **478** (2002) 511-526.

[15] HADES Collaboration, TDR - A secondary pion beam for HADES experiment, *Internal HADES document*, 2013.

[16] I. Fröhlich *et al.*, Pluto: A Monte Carlo Simulation Tool for Hadronic Physics, *PoS ACAT* **076** (2007) [arXiv:0708.2382 [nucl-ex]].

[17] A. D. Brody *et al.*, π^-p Elastic Scattering in the c.m. Energy Range $1\,400-2\,000$ MeV, *Phys. Rev.* D **3** (1971) 2619-2637.

[18] Institute for Nuclear Studies - The George Washington University, SAID database, retrieved from `http://gwdac.phys.gwu.edu/analysis/pin_analysis.html` [online 2015, April 12].

[19] G. Höhler *et al.*, *Landolt-Börnstein - Group I Elementary particles, Nuclei and Atoms. Numerical Data and Functional Relationships in Science and Technology - New Series.* Volume 12b, 1988. Springer Verlag, ISBN 978-0387184128.

[20] National Institute of Standards and Technology - Physical Measurement Laboratory, PSTAR program, retrieved from `http://physics.nist.gov/PhysRefData/Star/Text/PSTAR.html` [online 2015, March 2].

List of Figures

List of Tables